Measurement of W-boson mass with the ATLAS detector at the LHC

Ghizlane Ez-zobayr

A dissertation submitted in partial fulfilment of the requirements for the Master's degree Physics Matter and Radiations, Specialisation Area of High Energy Physics

Supervisor:

Prof. Abdelilah Moussa
Prof. Abdelouahed El Fatimy
Prof. Yahya Tayalati
Dr. Hicham Atmani

:

Oujda, August 24, 2023

Dedicatory

Dedicated to my beloved mother **Bya Athmani**, whom I deeply miss. Her life was a blessing, and her loving memories are a treasure that I hold dear. Her prayers have always been with me, guiding and comforting me.

Abstract

This thesis describes the measurement of the W boson mass using the ATLAS detector based on the 2017 data-set recorded at a centre-of-mass energy of $\sqrt{s} = 5\ TeV$, corresponding to 256.827 pb^{-1} of integrated luminosity. Special runs with a low number of interactions per bunch crossing were conducted to improve the experimental resolution of the recoil measurement and the reconstruction of missing transverse momentum and transverse mass.

The primary emphasis of this research is on the leptonic decays of the W boson, specifically focusing on the channel $W^+ \to e^+\nu_e$. Additionally, the statistical uncertainty of the W boson mass measurement is evaluated in this study.

Keywords:

Résumé

Cette thèse décrit la mesure de la masse du boson W en utilisant le détecteur ATLAS avec les données enregistrées en 2017, à une énergie de centre de masse de $\sqrt{s} = 5\ TeV$ et une luminosité intégrée de 256,827 pb^{-1}. Des mesures spéciales avec un faible nombre d'interactions par croisement de faisceau ont été réalisées pour améliorer la résolution expérimentale de la mesure du recul et la reconstruction du moment transverse manquant et de la masse transverse.

L'accent principal de cette recherche est mis sur l'étude des désintégrations leptoniques du boson W, en particulier dans le canal $W^+ \to e^+\nu_e$. De plus, cette étude évalue l'incertitude statistique associée à la mesure de la masse du boson W.

Mots clés: masse du boson W, ATLAS, LHC, Modèle Standard

Acknowledgement

I would like to express my sincere gratitude to my supervisors, Prof.**Abdelilah Moussa** , Prof.**Abdelouahed El Fatimy**, Prof.**Yahya Tayalati**, Dr.**Hicham Atmani**, for their invaluable guidance, support, and expertise throughout my thesis journey. Your collective wisdom and mentorship have been instrumental in shaping my research and academic growth. I am truly grateful for the opportunity to learn from each of you and for the valuable insights you have provided. Your dedication and commitment to my success have been truly inspiring. Thank you for your unwavering support and for believing in me.

I would also like to thank my colleagues, Mr.**Yassin Bimgdi**, Mr.**Mohamed Reda Mekouar** and Mr.**Amine Meskar**, for their friendship, support, and fruitful collaborations. Their input and discussions have greatly enriched my research and made the journey more enjoyable.

Finally, I would like to express my deepest appreciation to my sister Mme.**Fatima Ez-zobayr** for her unwavering support, love, and encouragement throughout this journey. Her belief in me has been a constant source of motivation, and I am truly grateful for her presence in my life.

I am grateful to all the individuals mentioned above for their contributions and support, without which this thesis would not have been possible.

Contents

List of Figures

List of Tables

Introduction

After the discovery of the W and Z bosons at the Super Proton Synchrotron (SPS) at CERN, which are responsible for weak interactions, significant efforts have been devoted to precisely measuring their properties. This aim is driven by the desire to test the consistency of the Standard Model.

The mass of the W boson is a highly significant parameter of the Standard Model, and its measurement with high accuracy serves as a crucial test of the model's internal consistency. Multiple experiments have been dedicated to achieving the highest possible precision in determining the W boson's mass. Among these experiments, the ATLAS detector at the LHC.

In this thesis we focus on the measurement of W boson mass using data obtained from the ATLAS detector at the LHC. The data was collected at a center-of-mass energy of 5 TeV, corresponding to integrated luminosities of 256.827 pb^{-1} during special runs with a low number of interactions per bunch crossing.

The primary focus of this research is on the leptonic decays of the W boson, where the charged decay products, electron, is accompanied by a neutrino. While the neutrino cannot be directly measured in the detector, it can be indirectly determined by considering the lepton and the hadronic system that recoils against the W boson.

Chapter 1 provides an overview of the Standard Model. Additionally, it discusses the production of W bosons in proton-proton collisions at the LHC. Furthermore, a brief historical account of W boson mass measurements is presented, with a particular focus on the latest results published by the ATLAS collaboration.

Chapter 2 presents a comprehensive overview of the experimental setup utilized for data collection in this thesis, providing a detailed description of the ATLAS detector at the LHC. Furthermore, it delves into the reconstruction process of critical objects that play a significant role in determining the mass of the W boson.

Chapter 3 describes the W boson mass measurement using two different approaches: the templates method, which was developed before for the Run 1 analysis, and the use of unfolded distributions for our variables of interest. This chapter, focuses on evaluating the statistical uncertainty of the W boson mass measurement using the two aforementioned approaches, discussing the differences between the two methods.

Chapter 1

Theoretical context

1.1 Introduction

Throughout ancient times, people have attempted to provide answers to the following questions: what is matter made of? Are there fundamental elements? What is our universe made of? Particle physics, the branch of science that is interested in the research of the ultimate components of matter and their modes of interaction, provides the answers to these concerns. It allows us to understand the world around us by describing the fundamental constituents of matter, which is done within a quantum theory of fields called the Standard Model (SM), which was developed during the 1960s.

The standard model of particle physics and its attributes are discussed in this chapter. We then shift our focus to the physics aspects, characteristics, production, and decay modes of the W boson. Additionally, we examine the previous results related to the measurement of the W boson's mass.

1.2 The standard model of particle physics

The standard model of particle physics [1][2][3] based on quantum physics and restricted relativistic theory, it classifies elementary particles into two types: fermions, which are considered to be particles of matter, and bosons, which are responsible for interactions. This model is based on a quantum field theory that has been formalized in the framework of gauge theories using local symmetry groups. The SM was developed with the gauge groups: SU(3)C, SU(2)L and U(1)Y, where SU(3)C is the special unitary group responsible for the strong interaction, SU(2)L is the special unitary group responsible for the weak interaction, and U(1)Y is the unitary group responsible for the electrodynamic interaction. Where the indices C, L, and Y are the color charge of quarks and gluons, the isospin, and the hypercharge,respectively. The SM uses the Lagrangian formalism, where each interaction is described by a Lagrangian density[4].

1.2.1 fermions

The fermions are the constituents of matter (atoms, cells, galaxies, etc.). They have a half-odd integer spin and obey the Fermi-Dirac statistics[5], hence their name, fermions. According to the Pauli exclusion principle[5], two identical fermions cannot exist in the same quantum state. According to the standard model, there are 12 fermions: 6 quarks and 6 leptons. To each fermion corresponds an antiparticle, that is to say, a particle of the same mass but with opposite quantum numbers and charge. Quarks and leptons are grouped into three generations, which differ from each other only by mass, higher at each generation. The first-generation particles form the constituents of stable matter (nuclei, atoms, molecules, etc.). In fact, second and third generation particles are unstable and decay quickly into first generation particles[4].

Leptons

The family of leptons consists of electrons (e), muons (µ), tauons (τ), neutrinos (ν) and their antiparticles, of spin 1/2. Leptons are insensitive to the strong interaction.The following table gathers the characteristics of leptons :

Name	Abbreviation	Mass MeV	Charge [e]	Generation
Electron	e	0.511	-1	I
Neutrino e	ν_e	$< 2.10^{-9}$	0	I
Muon	μ	105.658	-1	II
Neutrino µ	ν_μ	$<0.19.10^{-3}$	0	II
Tau	τ	1667.82	-1	III
Neutrino τ	ν_τ	<0.0182	0	III

Table 1.1: The list of leptons constituting the matter in the SM and their characteristics [6].

Quarks

Quarks are also in the number of six [4], u (up), d (down), c (charme), s (strange), t (top) and b (bottom). Quarks are sensitive to strong interaction, and they have charges that are fractions of the charge of an electron (±1/3e and ±2/3e), in addition they are characterized by a color charge that is introduced in order to distinguish quarks that appear to be in the same quantum state (Δ++, Δ− and Ω-). The existence of quarks has been experimentally confirmed by the study of the structure of the proton. Originally, the model contained only three quark flavors, up(u), down(d) and strange(s), but as early as 1970, Glashow, Iliopoulos and Maiani postulated the existence of a fourth quark: the charm "c", which was confirmed in 1974 by the discovery of the meson c$\bar{c}$ (charmonium) called J/ψ by Richter and Ting independently[7]. Also, quark b was observed as for quark "c" in mesons b$\bar{b}$ as early as 1977 and later in hadrons with quarks b. The t quark was first observed in the p$\bar{p}$ interactions at Fermilab in 1996.Quarks are grouped into pairs: (u, d),(c, s) (t, b)[7]. The following table shows the characteristics of quarks :

Name	Abreviation	Mass MeV	Charge [e]	Generation
Up	u	2.3	+2/3	I
Down	d	4.8	-1/3	I
Charm	c	1.275	+2/3	II
Strange	s	95	-1/3	II
Top	t	173.5	+2/3	III
Beauty	b	4.65	-1/3	III

Table 1.2: The list of quarks constituting the matter in the SM and their characteristics[6].

1.2.2 Bosons

In addition to the fermions, there are 13 elementary bosons [4]. Bosons have an integer spin and obey the Bose-Einstein statistics[5], The family of bosons includes: photons, gluons, Z and W bosons (discovered at CERN in 1983), the Higgs boson (discovered at CERN in 2012). Bosons act as mediators (messengers) of three of the four fundamental interactions: electromagnetic interaction, weak interaction and strong interaction. Thus an interaction between two elementary particles is accompanied by an exchange of bosons.

Interactions

Within the framework of the Standard Model[4], three of the four fundamental interactions are described: the electromagnetic, the weak, and the strong interactions. The table 1.3provides an overview of these interactions along with their respective characteristics. However, it is worth noting that the Standard Model does not include the gravitational force, which is one of its limitations :

The electromagnetic interaction: it acts between all particles possessing an electric charge, the photon, a non-massive boson, is the carrier particle of this interaction which gives the electromagnetic interaction an infinite range. It is responsible for the cohesion of atoms by linking the electrons and the nucleus of atoms.

The weak interaction : it acts on all fermions. The massive gauge bosons $W\pm$ and Z^0 are the mediators of this interaction. It is responsible for the radioactivity that transforms a neutron into a proton or vice versa. Its range is about one hundredth of a femtometer (fm).

The strong interaction: it acts on particles with a color charge (quarks, antiquarks and gluons). The 8 gluons, non-massive bosons, are the mediators of this interaction. The latter is responsible for the confinement of quarks in hadrons. Its range is of the order of a femtometer.

Interaction	Boson	Charge [e]	Spin	Mass GeV	sensitive particles
Electromagnetic	photon (γ)	0	1	<10^{-27}	Quarks and charged leptons
	W+	+1	1	80.385	Quarks and leptons
Weak	W-	-1	1	80.385	Quarks and leptons
	Z^0	0	1	91.1876	Quarks and leptons
Strong	gluons (g)	0	1	0	Quarks
Electroweak	H	0	0	125.4	Massive particles

Table 1.3: The list of interactions and mediator bosons in the MS and their characteristics[6].

1.2.3 Quantum Electrodynamics (QED)

Quantum Electrodynamics [8] is the quantum theory that describes the electromagnetic interaction between charged particles using the relativistic Lagrangian formalism. According to this theory, electric charges interact through the exchange of virtual photons. U(1) is the symmetry group that governs this theory.
For a free fermionic field ψ, the Dirac Lagrangian is given by [8] :

$$\mathcal{L} = \bar{\psi}(x)(i\gamma^{\mu}\partial\mu - m)\psi(x) \tag{1.1}$$

Where γ^{μ} are the Dirac matrices, $\bar{\psi} = \psi^{\dagger}\gamma^{0}$ is the Dirac adjoint, and m is the particle's rest mass. Under the transformation $\psi \to e^{-i\alpha(x)}\psi$ corresponding to the abelian symmetry group U(1), the Lagrangian becomes:

$$\mathcal{L} = \bar{\psi}(x)i\gamma^{\mu}\partial_{\mu}\psi(x) + \gamma^{\mu}\bar{\psi}(x)\partial_{\mu}(\alpha(x))\psi(x) - m\bar{\psi}(x)\psi(x) \tag{1.2}$$

The principle of local gauge invariance imposes the replacement of the partial derivative by a covariant derivative:

$$\partial_{\mu} \to D_{\mu} = \partial_{\mu} + iqA_{\mu} \tag{1.3}$$

$$D_{\mu}\psi \to e^{-i\alpha(x)}D_{\mu}\psi \tag{1.4}$$

Where q is the electric charge and A_{μ} is a static field that transforms under U(1) as follows:

$$A_{\mu} \to A_{\mu} + \frac{1}{q}\partial_{\mu}\alpha(x) \tag{1.5}$$

In order to allow the propagation of the gauge field, a kinetic term must be added. The simplest gauge-invariant corresponding term is the following:

$$\mathcal{L}_{\text{cin}} = -\frac{1}{4}F_{\mu\nu}F^{\mu\nu} \qquad with \qquad F_{\mu\nu} = \partial_{\mu}A_{\nu} - \partial_{\nu}A_{\mu} \tag{1.6}$$

Finally, we obtain the expression of the Lagrangian of quantum electrodynamics:

$$\mathcal{L}_{\text{QED}} = \bar{\psi}(x)i\gamma^{\mu}\partial_{\mu}\psi(x) - m\bar{\psi}(x)\psi(x) - \frac{1}{4}F_{\mu\nu}F^{\mu\nu} - q\bar{\psi}(x)\gamma^{\mu}A_{\mu}\psi(x) \tag{1.7}$$

where:

$\bar{\psi}(x)i\gamma^{\mu}\partial_{\mu}\psi(x)$: Propagation of the fermion

$m\bar{\psi}(x)\psi(x)$: Mass of the fermion

$\frac{1}{4}F_{\mu\nu}F^{\mu\nu}$: Propagation of the boson

$q\bar{\psi}(x)\gamma^{\mu}A_{\mu}\psi(x)$: Boson-fermion interaction

1.2.4 Quantum chromodynamics (QCD)

Theoretically, the Standard Model is based on two main theories: quantum chromodynamics (QCD) and the electroweak theory. Quantum chromodynamics [9] is a theory proposed in 1973 by Politzer, Wilczek, and Gross to understand the structure of hadrons. Quantum chromodynamics describes the strong interaction between quarks through the exchange of gluons, based on the non-abelian gauge symmetry group SU(3)$_c$. This theory describes the conservation of color charge (can take on three values: red (R), green (G), and blue (B)) in the strong interaction. Therefore, each quark can be expressed as a triplet under SU(3)$_c$ symmetry :

$$\psi = \begin{pmatrix} \psi_R \\ \psi_G \\ \psi_B \end{pmatrix} \tag{1.8}$$

Considering a free fermionic field ψ, corresponding to a Lagrangian as in quantum electrodynamics. The field ψ transforms as follows:

$$\psi \;\rightarrow\; e^{-\frac{i}{2}\lambda^{a}\alpha^{a}}\psi \tag{1.9}$$

With λ^a are the Gell-Mann matrices[9], in the QCD framework, the covariant derivative and the tensor $F^a_{\mu\nu}$ which translates the kinetic term are written of the following form:

$$D_{\mu} = \partial_{\mu} - \frac{i}{2}\lambda^{a}A^{a}_{\mu} \tag{1.10}$$

$$F^{a}_{\mu\nu} = \partial_{\mu}A^{a}_{\nu} - \partial_{\nu}A^{a}_{\mu} + g_{s}f^{abc}A^{b}_{\mu}A^{c}_{\nu} \tag{1.11}$$

With A^a_{ν} being the fields of the 8 gluons, g_s the strong coupling constant ($g_s^2 = 4\pi\alpha_s$), and f^{abc} being the structure constants of the SU(3)$_C$ group. Finally, the expression of the Lagrangian of quantum chromodynamics is written as follows:

$$\mathcal{L}_{QCD} = \bar{\psi}i\gamma^{\mu}\partial\mu\psi - m\bar{\psi}\psi + \bar{\psi}\gamma^{\mu}\frac{g_s}{2}\lambda^{a}A^{a}_{\mu}\psi - \frac{1}{4}(\partial_{\mu}A^{a}_{\nu} - \partial_{\nu}A^{a}_{\mu})^{2} - \frac{1}{2}(\partial_{\mu}A^{a}_{\nu} - \partial_{\nu}A^{a}_{\mu})g_{s}f^{abc}A^{b}_{\mu}A^{c}_{\nu} - \frac{1}{4}g_s^2(f^{abc}A^{b}_{\mu}A^{c}_{\nu})^{2} \tag{1.12}$$

where :

$\bar{\psi}i\gamma^{\mu}\partial_{\mu}\psi$: The kinetic term of the field ψ ;

$m\bar{\psi}\psi$: The mass term of the field ψ ;

$\bar{\psi}\gamma^{\mu}\frac{g_s}{2}\lambda^{a}A^{a}_{\mu}\psi$: The interaction between the field ψ and the gluon field A^a_{μ} ;

$\frac{1}{4}(\partial_{\mu}A^{a}_{\nu} - \partial_{\nu}A^{a}_{\mu})^{2}$: The kinetic term of the gluon field A^a_{μ} ;

$\frac{1}{2}(\partial_{\mu}A^{a}_{\nu} - \partial_{\nu}A^{a}_{\mu})g_{s}f^{abc}A^{b}_{\mu}A^{c}_{\nu}$: The term that characterizes the interaction of 3 gluons;

$\frac{1}{4}g_s^2(f^{abc}A_\mu^b A_\nu^c)^2$: The term that characterizes the interaction of 4 gluons.

QCD has two major properties: asymptotic freedom and quark confinement. Confinement means that quarks are confined (prisoners) within hadrons, which can be explained by an anti-screening effect opposite to the screening effect of electric charge. Indeed, the color charge of quarks increases as one moves away from them, since the gluons that connect them are themselves colored, and their number increases with distance. This anti-screening effect thus increases with distance and decreases with the energy of the particles that interact with the quark. When the energy tends towards infinity, quarks interact like free particles. This is called asymptotic freedom (the opposite phenomenon to confinement).

1.2.5 Electroweak theory and Higgs mechanism

According to the 'GWS theory' developed by Glashow, Weinberg, and Salam [1][2][3] in the 1960s, electromagnetic and weak interactions are unified within the framework of a single theory called 'the electroweak theory'. It is a quantum field theory based on a gauge group of SU(2)L × U(1)Y, with the exchange of four mediator bosons: photon, Z, W+ and W-. The lagrangian of the electroweak theory is described as follows:

$$\mathcal{L}_{EW} = \bar{\psi}_L(i\gamma^\mu D_\mu)\psi_L + \bar{\psi}_R(i\gamma^\mu D'_\mu)\psi_R - \frac{1}{4}F^A_{\mu\nu}F^{\mu\nu}_A - \frac{1}{4}B_{\mu\nu}B^{\mu\nu} \tag{1.13}$$

The first two terms represent the interactions between particles, mediated by gauge bosons, while the last two terms represent the interactions between the gauge fields themselves. The quantities $F^A_{\mu\nu}$ and $B_{\mu\nu}$ are gauge antisymmetric tensors constructed from the gauge fields B_μ and W^a_μ.

The covariant derivative D is given by :

$$D_\mu = \partial_\mu + igT^aW^a_\mu + ig'\frac{1}{2}T_Y B_\mu \tag{1.14}$$

Where T^a and T_Y are the generators of SU(2)L and U(1)Y respectively. The variables g and g' are the coupling constants of SU(2)L and U(1)Y, respectively, related as follows:

$$\tan\theta_W = \frac{g'}{g} \tag{1.15}$$

where θ_W is the electroweak mixing angle

Using θ_W, the gauge bosons can be written as linear combinations of the gauge fields:

$$\gamma : A_\mu = \cos\theta_W B_\mu + \sin\theta_W W^3_\mu \tag{1.16}$$

$$Z^0 : Z_\mu = -\sin\theta_W B_\mu + \cos\theta_W W^3_\mu \tag{1.17}$$

$$W^\pm : W^\pm_\mu = \frac{1}{\sqrt{2}}\left(W^1_\mu \mp iW^2_\mu\right) \tag{1.18}$$

According to the electroweak lagrangian[10], in order to preserve the SU(2)L⊗U(1)Y gauge symmetry, it is necessary that the bosonic field must be massless. However, experimental observations have shown the existence of massive bosons, which poses a problem. To solve this conflict, the Brout-Englert-Higgs mechanism was proposed in 1964. This mechanism consists in adding an additional scalar boson called the Higgs boson and generating a "Higgs field" which interacts with W and Z bosons, providing them with masses. This mechanism is called "spontaneous symmetry breaking". In order to explain this mechanism, it is necessary to introduce a new doublet of complex scalar fields :

$$\Phi_H = \begin{pmatrix} \Phi^+ \\ \Phi^0 \end{pmatrix}$$
$$\Phi^+ = \frac{\phi_1 + i\phi_2}{\sqrt{2}} \tag{1.19}$$
$$\Phi^0 = \frac{\phi_3 + i\phi_4}{\sqrt{2}}$$

where ϕ_i are real fields, and the Lagrangian of the Higgs field can be expressed as follows:

$$\mathcal{L}_{\text{scalar}} = (D_\mu \Phi_H)^\dagger (D^\mu \Phi_H) - V(\Phi_H) \tag{1.20}$$

Where $(D^\mu \Phi_H)^\dagger (D_\mu \Phi_H)$ contains the interaction between the Higgs and gauge bosons, and the second term is a potential of the following form:

$$V(\Phi_H) = -\mu^2 |\Phi_H|^2 + \lambda \left(|\Phi_H|^2 \right)^2$$

where μ and λ are two free parameters.

The mass term of the Higgs boson is expressed as follows: $m_H^2 = 2|\mu|^2 = 2\lambda v^2$, while the masses of the gauge bosons are written as follows:

$$m_W^2 = \frac{1}{4} g^2 v^2, \quad m_Z^2 = \frac{1}{4}(g^2 + g'^2) v^2 \tag{1.21}$$

1.3 The W boson

In 1983, the UA1 (Underground Area 1) and UA2 (Underground Area 2) collaborations discovered the W boson, which is the mediator of the weak interaction. This force is responsible for β decay. The discovery was made in proton-antiproton collisions at the SPS (Super Proton Synchrotron) collider[11].
After this discovery, significant efforts were made to measure the properties of the W boson with high precision to test the coherence of the Standard Model. In fact, the Standard Model[4] has 25 free parameters to describe the particles and their interactions. Some of these parameters are directly measured with considerable precision, while others are constrained by measurements of physical quantities related by the theory. For example, the mass m_W of the W boson is related to the masses of the Z boson, the Higgs boson, and the top quark, taking into account radiative corrections. The precise measurement of the mass of the Z boson was obtained by the LEP experiments, and the discovery of the Higgs boson in 2012 at the LHC[12] allowed for the theoretical prediction of the mass of the W boson. The comparison between predicted and measured values is considered a reliable test of the validity of the Standard Model.

1.3.1 W boson production at the LHC

According to the Drell-Yan process [13], first described in the 1970s, quarks-antiquark annihilations are the dominant process for the production of W bosons at the LHC. Figure 1.1 illustrates this mechanism:

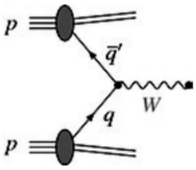

Figure 1.1: Mechanism of W boson production in hadronic colliders. [14]

The W^+ bosons [15] are mainly produced from a u$\bar{d}$ quark-antiquark pair, while the W^- bosons are mainly produced from $\bar{u}$d collisions.

To create a W boson in hadronic collisions [13], two partons, denoted q_1 and $\bar{q}_2$, must collide. Each carries a fraction x_1 and x_2 of the four-momentum of their respective protons P_1 and P_2. The transferred momentum, denoted Q^2, is calculated using the formula $Q^2 = (p_1 + p_2)^2 = (p_3 + p_4)^2 = sx_1x_2$, where p_1 and p_2 correspond to the momenta of the initial partons, and p_3 and p_4 correspond to those of the final particles e and ν_e. The energy of the protons in the center-of-mass frame is represented by the square root of s, that is $\sqrt{s} = P_1 + P_2$. If the production of the W boson occurs resonantly, then Q^2 is equal to the mass of the W boson, denoted m_W.
According to the parton model, the production cross section $\sigma_{pp\to W}$ is calculated as the product of the partonic cross section $\sigma_{q\bar{q}\to W}$ and the parton distribution functions $f_i(x_i, Q^2)$, which represent the probability of finding a parton i with momentum fraction x_i in a proton, for a given momentum transfer. The cross section can be calculated using the following formula:

$$\sigma_{\mathrm{pp}\to\mathrm{W}} = \sum_{q,\bar{q}'} \int dx_1 dx_2 f_1(x_1, Q^2) f_2(x_2, Q^2) \sigma_{\mathrm{q\bar{q}}\to\mathrm{W}} \tag{1.22}$$

where

$$\sigma_{\mathrm{q\bar{q}}\to\mathrm{W}} = 2\pi \left|V_{q\bar{q}}\right| G_F M_W^2 \frac{1}{\sqrt{2}} \delta(x_1 x_2 s - M_W) \tag{1.23}$$

where $|V_{q\bar{q}}|$ is the CKM (Cabibbo-Kobayashi-Maskawa) matrix element. This cross section increases with energy in the center-of-mass frame.

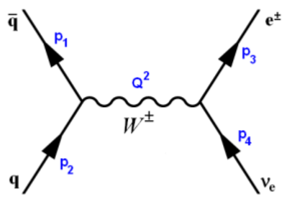

Figure 1.2: Feynman diagram of the production of a W± boson decaying into eν.[15]

1.3.2 The decay modes of the W boson

The uncertainty on the mass of the W boson is related to its short lifetime ($\tau = 3\times10^{-25}$ s), and the measurement of the mass of this boson in particle colliders is achieved using its decay products. The W boson has the ability to decay through two different modes: the leptonic mode, where it splits into a lepton and its associated neutrino, and the hadronic mode, where it splits into two quarks. Table 3.2 presents the branching ratios for each of these decay channels.

Decay	Channel	Branching ratio
	$W \to e + \nu_e$	$10.75 \pm 0.13\%$
Leptonic	$W \to \mu + \nu_\mu$	$10.57 \pm 0.15\%$
	$W \to \tau + \nu_\tau$	$11.25 \pm 0.20\%$
Hadronic	$W \to q + \bar{q}'$	$67.60 \pm 0.27\%$

Table 1.4: The branching ratios of the different decay channels of the W boson. [6]

1.3.3 W boson mass

Prediction in the SM

The mass of the Higgs boson, the weak mixing angle θ_W, and the coupling constants (g, g') are the three fundamental parameters of the electroweak interactions, as was demonstrated in the section 1.2.5. The W boson mass can be represented at the lowest order of the EW theory as a function of the Z boson mass, the Fermi constant G_F, and the fine structure constant($\alpha = \frac{e^2}{4\pi}$).The mass of the Z boson m_Z, which was accurately ascertained from the Z lineshape scan at LEP1[16], the Fermi constant G_F[17], and the fine-structure constant are taken to be these values:

$$\alpha_{em}^{-1} = 137.035999074(44)$$
$$G_F = 1.1663787(6) \times 10^{-5} GeV^{-2}$$
$$m_Z = 91.1876(21) GeV$$

At this level[18], the W boson mass in eq.1.21 can be rearranged via these parameters:

$$m_W = \sqrt{\frac{\pi\alpha}{\sqrt{2}\,G_F}}\frac{1}{\sin\theta_W} \tag{1.24}$$

$$\text{with : } \frac{g^2}{8m_W^2} \equiv \frac{1}{2v^2} = \frac{G_F}{\sqrt{2}}$$

It predicts a W mass value of $m_W = 80.939 \pm 0.0026$ GeV. At higher-order corrections[18] The W-boson mass depends on the gauge couplings and the masses of the heavy particles in the SM. The W boson's mass can be stated using the other SM parameters as follows[19]:

$$m_W = \sqrt{\frac{\pi\alpha}{\sqrt{2}\,G_F}}\frac{1}{\sin\theta_W}\frac{1}{\sqrt{1-\Delta r}} \tag{1.25}$$

where Δr takes all the higher-order corrections into account,it depends on the top-quark mass quadratically and on the Higgs and Z masses logarithmically :

$$\begin{aligned} \Delta r &= -\frac{\cos^2\theta_W}{\sin^2\theta_W}\Delta\rho + \frac{\alpha}{3\pi}\left[\frac{1}{2} - \frac{\sin^2\theta_W}{3(1-\tan^2\theta_W)}\right]\log\frac{m_H^2}{m_Z^2} + \ldots \sim 1\% \\ \Delta\rho &= \frac{\alpha m_t^2}{\pi m_Z^2} - \frac{\alpha}{4\pi}\log\frac{m_H^2}{m_Z^2} + \ldots \sim 1\% \end{aligned} \tag{1.26}$$

In summary, $\Delta r = \Delta r(\alpha, m_z, m_t, m_H)$ includes the top quark and Higgs masses which are not present at the tree level expression, in extended theories, this quantity receives contributions from additional particles and interactions. All those effects make the W mass boson a highly significant parameter of the SM. Obtaining an accurate measurement of the W boson mass, by comparing the experimental measurement of m_W to the theoretical predictions, would be a crucial test of the internal consistency of the SM and any failure might indicate the presence of new physics beyond the Standard Model. A global fit [20] of the electroweak parameters is used to calculate the W boson mass at higher order corrections :

$$m_W = 80.359 \pm 0.006\,\mathrm{GeV}$$

Experimental determinations of W boson mass

Since the W boson's discovery in 1983 many experiments have measured its mass,with the aim of inceasing the precision as much as possible, namely at LEP (Large Electron-Positron collider),Tevatron and the LHC.

In electron-positron collisions[21], the W bosons are pair-produced by electron-positron annihilation for $\sqrt{s} = 2m_W$ .The bosons then quickly decay into a final state of four fermions: hadronic ($q\bar{q}q'\bar{q}'$), leptonic ($l\nu l'\nu'$), and semi-leptonic ($qq'l\nu$).
The mass of the W boson can be determined in two different ways:

- The first method involves measuring the total production cross-section of W-pair near the W-pair production threshold and comparing the measured cross-section with MC (Monte-Carlo) templates to extract the mass and width of the boson.
- The second method involves reconstructing the invariant mass from the decay products' moments of the pair. By fitting the invariant mass distribution with MC templates, the W boson's mass and width can be extracted. This method requires a lot of statistics and is mainly used beyond the pair production threshold.

The W bosons are produced at the $p\bar{p}$ colliders [22] from the protons' quarks. For the mass measurement, the quantities perpendicular to the beam direction are employed. At the TeVatron, W production is dominated by $q\bar{q}' \rightarrow W + X$ where X is initial state QCD radiation. the D∅ experiment (located at the Tevatron Collider at Fermilab) solely examines the $W \rightarrow e\nu$ channel, While the CDF (Collider Detector at Fermilab) experiment explores both the $W \rightarrow e\nu$ and $W \rightarrow \mu\nu$ decay modes.

At LEP, the measurements from all the experiments were combined to obtain an average value of 80.376 ± 0.033 GeV, as shown in the upper part of Figure 1.3. In 2012[23], the CDF and D∅ experiments reported their measurements of the mass of the W boson as 80.387 ± 0.019 GeV [24] and 80.375 ± 0.023 GeV [25], respectively. The lower part of Figure 1.3 displays the TeVatron measurements and their combination, resulting in a value of 80.387 ± 0.016 GeV. Assuming that there are no systematic uncertainties in common between the LEP and TeVatron measurements, the combined global average is currently estimated to be 80.385 ± 0.015 GeV.

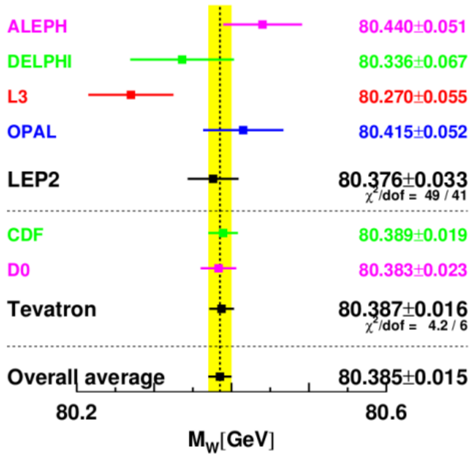

Figure 1.3: Measurements of the W-boson mass by the LEP and TeVatron experiments. [23]

In proton-proton collisions (LHC), the W is produced after the annihilation of a quark q and an anti-quark $\bar{q}'$ as was illustrated in the section 1.3.1, both valence (constituent quarks:one down quark and two up quarks) and sea (virtual quark-antiquark pairs) quarks participate in the process.However, valence-quark interactions are what mostly produce vector bosons in proton-antiproton collisions, whereas at least one sea quark is required in proton-proton collisions[22].

In 2017 [26], the ATLAS (A Toroidal LHC ApparatuS) Experiment at CERN (the European Organization for Nuclear Research) reported the first measurement of the W-boson mass using proton-proton collisions at a center-of-mass energy of 7 TeV collected during Run 1 in 2011. The value obtained was 80,370 GeV, with an uncertainty of 19 MeV. The measurement was based on the lepton transverse momentum (p_T^l) and transverse mass (m_T^W) distributions from $W \to l\nu$ using the template approach, which will be discussed in Chapter 3.

On 23 March 2023[27], the ATLAS Collaboration announced a new result on the W-boson mass. They improved their initial measurement by using an advanced fitting technique based on a profile likelihood approach, which led to a reduction in several systematic uncertainties. The new value they found for m_W is 80,360 MeV, with an uncertainty of only 16 MeV. This measurement is 10 MeV lower than the previous ATLAS result and is in agreement with the Standard Model, as well as all other experimental results, except for the CDF measurement. Last year[28], the CDF Collaboration at Fermilab published an even more precise measurement of the W-boson mass, using the full dataset provided by the Tevatron collider. Their value was 80,434 GeV, with an uncertainty of 9 MeV. This differs significantly from the Standard Model prediction and suggests the possibility of either improvements to the SM calculation or extensions to the SM.

All these measures are represented in the figure1.4 :

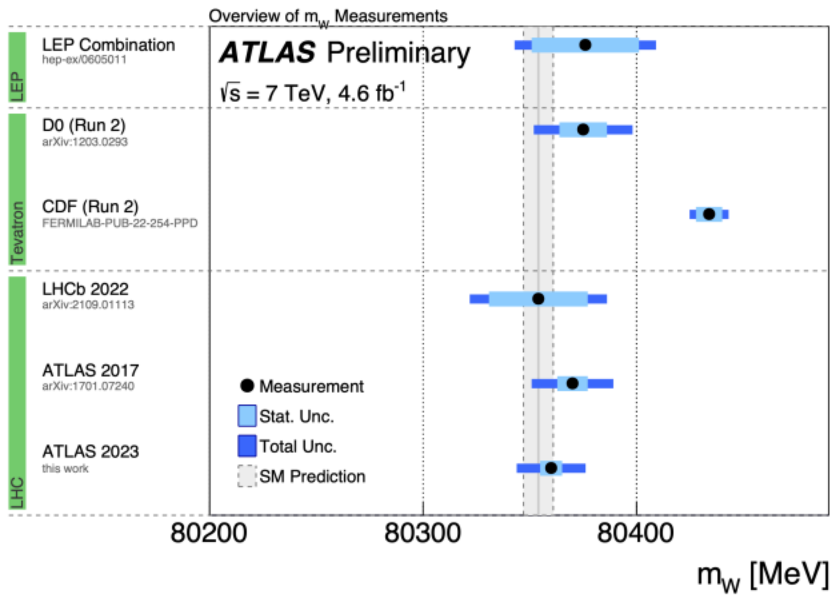

Figure 1.4: Comparison of the measured value of the W boson mass with other published results. The vertical bands show the Standard Model prediction, and the horizontal bands and lines show the statistical and total uncertainties of the results [27]

1.4 Conclusion

The Standard Model is a unified theory that describes elementary particles and their interactions, combining quantum chromodynamics and the electroweak model. Experimental investigations have extensively verified its theoretical predictions, including the discovery of the Higgs boson. However, the model has limitations in explaining certain phenomena and fundamental questions, such as dark matter and neutrino oscillation.

The mass of the W boson is a highly significant parameter of the Standard Model, and its measurement with high accuracy serves as a crucial test of the model's internal consistency. Multiple experiments have been dedicated to achieving the highest possible precision in determining the W boson's mass. Among these experiments, the ATLAS detector at the LHC. In the upcoming chapter, a detailed description of the ATLAS experiment will be presented, offering a comprehensive overview that includes its objectives and general information.

Chapter 2

The Experimental Setup: The ATLAS experiment at the LHC

2.1 Introduction

The experimental context holds a paramount significance in scientific research, as it enables the verification of theoretical predictions. In the field of particle physics, several particles were predicted in the 1970s, such as the $W^{\pm}$,Z^{0}, and Higgs bosons, as well as the top quark. However, these predictions had no scientific value until they were experimentally verified. Over the years, particle accelerators such as the LEP, Tevatron, and more recently the LHC have allowed for the detection and verification of the existence of these particles. However, there are still unanswered questions in the standard model of particle physics, such as dark matter and matter-antimatter asymmetry. To answer these questions, it is necessary to use very powerful particle accelerators, such as the LHC. The latter is currently the most powerful particle accelerator in operation, located at CERN since 2010. The results presented in this dissertation are based on data collected during Run 2 by the ATLAS experiment at the Large Hadron Collider. This chapter provides an overview of the LHC and of the ATLAS experiment.

2.2 The Large Hadron Collider

The LHC[29] is a circular particle accelerator located near Geneva, Switzerland, with a circumference of 27 kilometers and housed in a tunnel dug approximately 100 meters deep. The LHC is a proton-proton and heavy-ion accelerator designed to provide center-of-mass energies and luminosities that have never before been possible for the study of novel physics. It is the most powerful particle accelerator ever built and is the successor of the Large Electron Positron (LEP) accelerator. The LHC consists of two rings where proton (or lead ion) beams are circulated in two different vacuum tubes, traveling in opposite directions. It is segmented into eight octants (as shown in Figure 2.1), with collision points situated in the middle of each octant. To accelerate the protons in each beam, the LHC employs a ring made up of a series of radio-frequency cavities, while superconducting dipole magnets (approximately 1232 in number) are utilized to focus and bend the beams, generating a magnetic field of 8.63 Tesla. In the LHC, the particles are grouped into about 2000 bunches in each beam, which can contain $10^{1}1$ particles per bunch, reaching an energy up to 6.5 TeV per beam, corresponding to a velocity very close to the speed of light (0.999 999 99 c).Therefore, the beams collide with a center of mass energy up to 13 TeV and a collision frequency of every 25 nanoseconds[30].

2.2.1 The LHC acceleration chain

Particles are not immediately injected into the LHC. Instead, they are first accelerated through a series of lower-energy accelerators [31], each one increasing the energy of the colliding beams. This process can lead to a center-of-mass energy of up to 14TeV for protons and 5.5 TeV per nucleon pair for heavy ions. The protons are first extracted and separated from ionized hydrogen using an electric field. They are then brought to an energy of 50 MeV by the LINAC2 linear accelerator before being injected into the BOOSTER, the first circular accelerator which further increases their energy up to 1.4 GeV. The Proton Synchrotron (PS) and Super Proton Synchrotron (SPS) then increase the energy to 25 GeV and 450 GeV, respectively. Finally, the proton beams are injected into the LHC where they are accelerated to their maximum energy of 6.5 TeV.

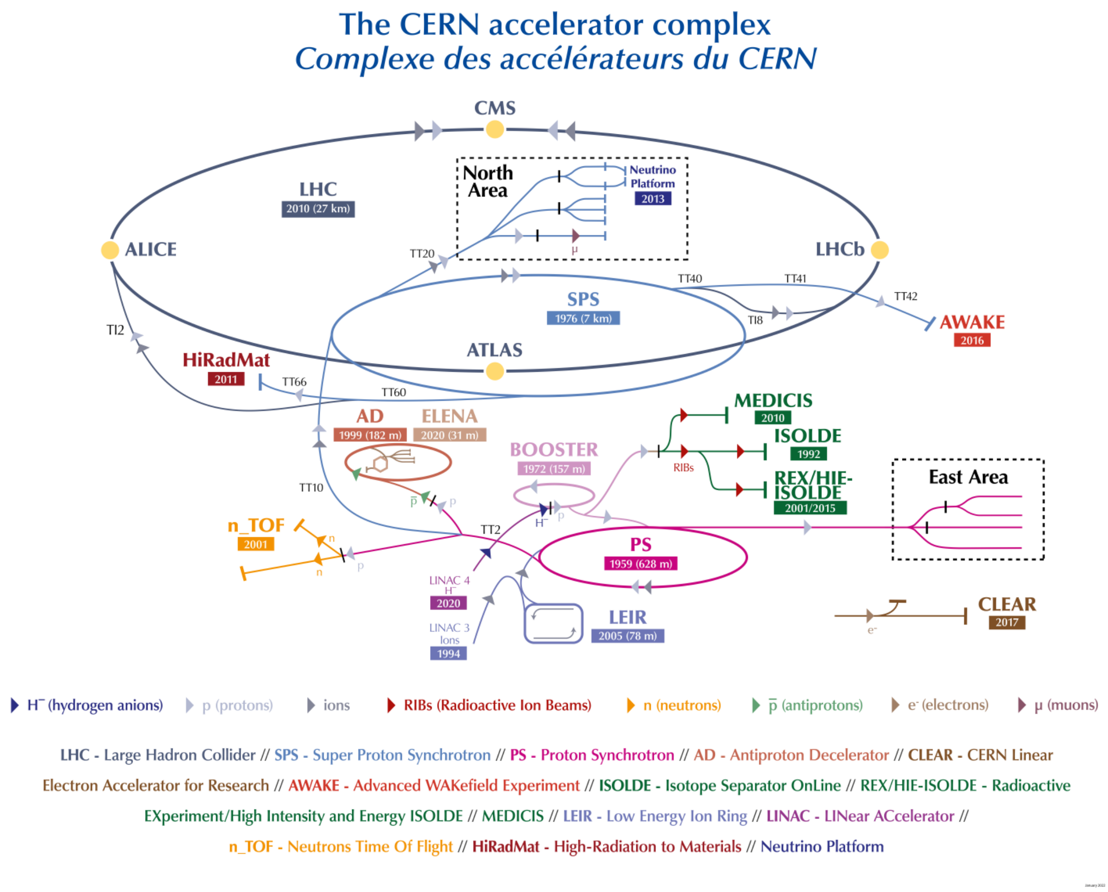

Figure 2.1: Illustration of the LHC accelerator complex[32].

2.2.2 LHC performance

We can evaluate the performance of the LHC based on two key factors. The first is the center of mass-energy, which provides an estimate of the available energy for generating new processes[33]. The second factor is the instantaneous luminosity[34], which quantifies the number of collisions that can be generated per unit time and area, (expressed in units

$cm^{-2}s^{-1}$). In terms of beam parameters, the instantaneous luminosity can be expressed as:

$$\mathcal{L}_{\text{int}} = \frac{N_b^2 n_\text{b} f_\text{r} \gamma}{4\pi \epsilon_n \beta^*} \times F \tag{2.1}$$

Where N_b (the number of protons per bunch), n_b (the number of bunches per beam), f_r (the revolution frequency), γ (the Lorentz factor of special relativity), ϵ_n (the transverse emittance of the beam, which corresponds to the dispersion of the beam in the phase space position-pulse in the transverse plane), β^* (the beta function at the point of collision, which quantifies the amplitude of the envelope of the beam), and F (a geometric factor that depends largely on the crossing angle of the beams). Another quantity that is useful in quantifying the amount of data delivered by or recorded by an experiment is the integrated luminosity L. This quantity corresponds to the integral of instantaneous luminosity over time, and is expressed in inverse femtobarns fb : Lint = $\int \mathcal{L}_{inst}(t).dt$ The integrated luminosity is related to the number of events obtained for a physical process with a production cross section σ , via : $N_{\text{event}} = \sigma \times L_{\text{int}}$.
Another important factor in our analysis is the pileup[35], which refers to the number of inelastic collisions between protons per bunch crossing. The average number of proton-proton collisions per bunch crossing is denoted by μ :

$$\mu = \frac{\mathcal{L}_{\text{inst}} \cdot \sigma_{\text{inel}}}{n_b \cdot f} \tag{2.2}$$

Where σ_{inel} is the total inelastic cross section, n_b is the number of colliding packets and f represents the revolution frequency of the LHC.Our analysis utilizes a specific dataset that is distinguished by its low pileup value ($\mu = 2$). This dataset was collected during Run 2 in 2017 and 2018.

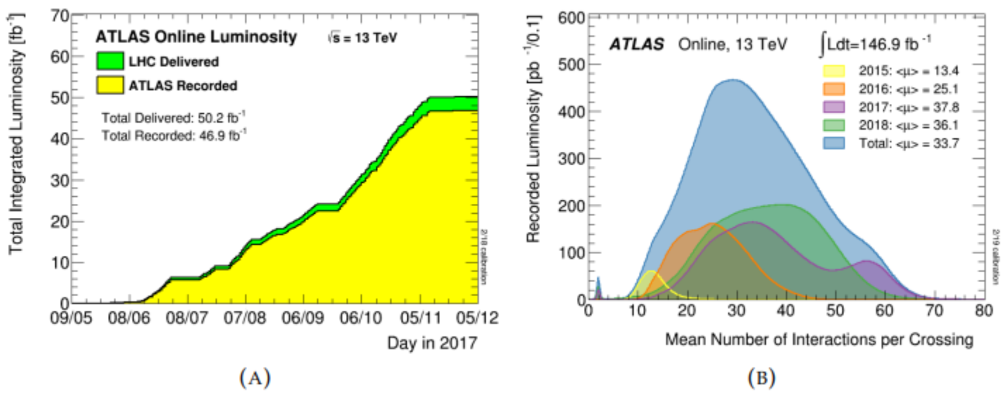

Figure 2.2: (A) Integrated luminosity delivered (in green) and recorded (in yellow) by the ATLAS experiment during stable beams for proton-proton collisions at a center-of-mass energy of 13 TeV, plotted as a function of time. (B) Mean number of interactions per crossing $< \mu >$ per year in Run 2 [35].

2.2.3 LHC experiments

Four experiments are recipients of particle collisions delivered by the LHC:

ATLAS[36] (A Large Toroidal LHC ApparatuS) and **CMS**[37] (Compact Muon Solenoid) : are general-purpose detectors, designed to detect all types of particles produced in proton-proton collisions.
LHCb[38] (A Large Ion Colliding Experiment) : The purpose of this experiment is to investigate CP violation (where C stands for charge and P for parity), study matter-antimatter asymmetry, and search for new phenomena in the sector of b-quarks.
ALICE[39] (A Large Ion Collider Experiment) : Its main objective is to investigate the properties of a quark-gluon plasma by carrying out collisions of heavy Pb-Pb ions.

2.3 The ATLAS Experiment

The ATLAS detector[36] (A Toroidal LHC Apparatus) is a general-purpose detector installed at the LHC (Large Hadron Collider). With its 4π steradian acceptance, the ATLAS detector is designed to cover a wide solid angle. It consists of multiple sub-detectors, including inner detectors for tracking charged particles, a calorimetric system for measuring the energy of most particles, and muon spectrometers for recording the trajectories of muons. Additionally, the detector is equipped with solenoid and toroidal magnets that bend the paths of charged particles, allowing their momenta to be measured. Despite the different sub-detectors, all components of the ATLAS detector employ a unified coordinate system to determine the position or momentum of detected objects.

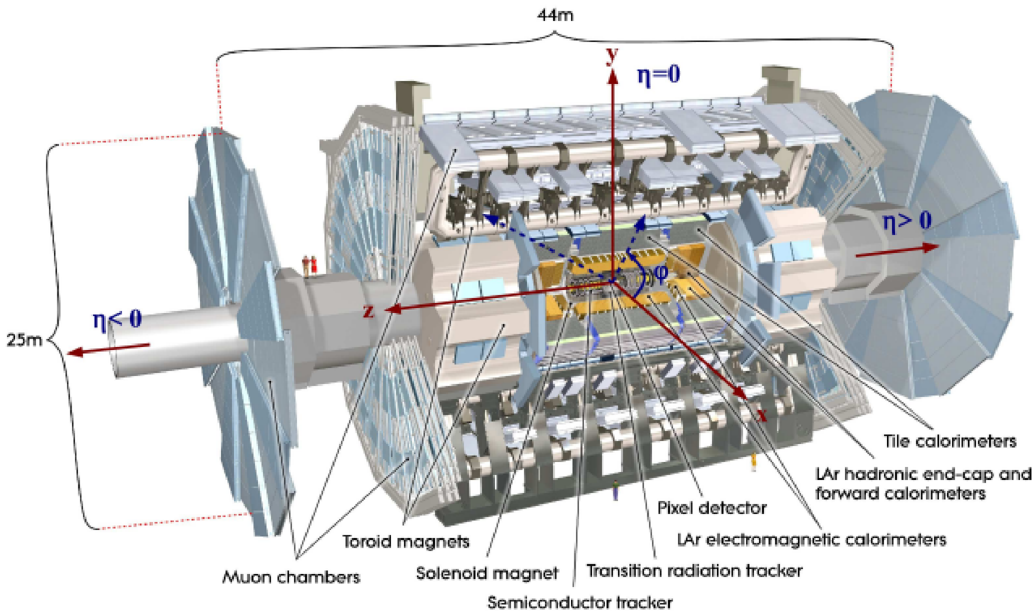

Figure 2.3: Overview of the ATLAS detector with its coordinate system and the variable η [40].

2.3.1 The Coordinate System

ATLAS uses a right-handed coordinate system[26],(as shown in Figure 2.4), where the nominal interaction point (IP) of pp collisions is defined as the origin of the ATLAS coordinate system, the z-axis aligned along the beam axis and the x and y axes defining the transverse plane of the detector. The convention is for the x-axis to point towards the center of the LHC. Angles θ and ϕ are used to describe the orientation relative to the z and x axes, respectively. In most cases, the variable θ is replaced by η, which represents the pseudo-rapidity and is defined as follows:

$$\eta = -\ln\left(\tan\frac{\theta}{2}\right) \tag{2.3}$$

Where the difference in pseudo-rapidity $\Delta\eta$ is Lorentz invariant under boosts along the longitudinal axis, Another important variable used to calculate the distances between two particles in the (η, φ) plane, the angular distance is defined as $\Delta R = \sqrt{\Delta\varphi^2 + \Delta\eta^2}$.

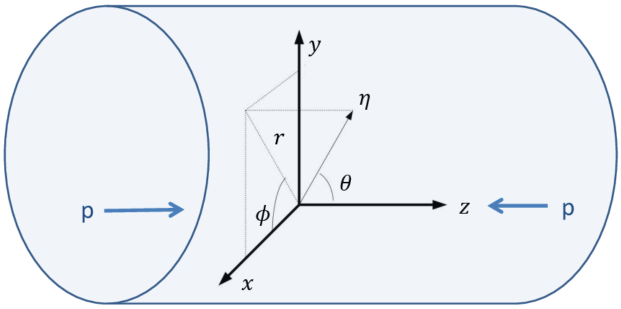

Figure 2.4: An overview of the ATLAS coordinate system[41].

2.3.2 Magnet systems

The ATLAS detector[36] two systems of superconducting magnets that curve the paths of charged particles, enabling their momentum measurements. The internal detector is immersed in a 2T magnetic field created by the solenoid magnet, while the toroidal system is responsible for bending the trajectories of muons in the outer region of the detector, known as the muon spectrometers. Figure 2.5 illustrates the arrangement of these magnet systems.

The solenoid magnet with a length of 5.8m and a diameter between 2.46 and 2.56m, generates a magnetic field of approximately 2T using a current intensity of 7730 kA. It is strategically positioned between the internal detectors and the electromagnetic calorimeter, designed to minimize material presence and optimize the performance of the calorimeter.

The toroidal magnet is divided into two sections: the barrel part, covering the central region of the detector with $|\eta| < 1.2$, and the cap part with $|\eta| < 2.7$. The barrel section consists of eight magnets, each 25.3m long and powered by an intensity of 20.5kA, generating a magnetic field of up to 2.5T. The smaller endcap sections produce magnetic fields reaching up to 3.5T.

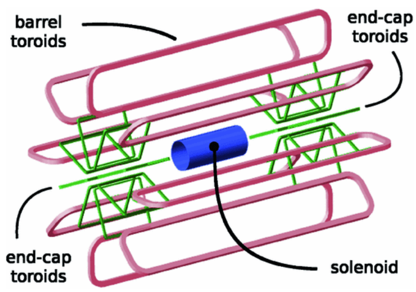

Figure 2.5: An overview of the ATLAS Magnet systems systems[41].

2.3.3 Inner Detector

Internal detectors[42] play a crucial role in measuring the trajectories and charges of charged particles. They are essential for particle identification and the reconstruction of primary and secondary vertices. The overall design of internal detectors, as depicted in Figure 2.6, comprises three sub-detectors: the pixel detector, the Semi-Conductor Tracker (SCT), and the Transition Radiation Tracker (TRT). These sub-detectors are exposed to the magnetic field produced by the solenoid magnet :

The pixel detector

The silicon pixel detector [43] consists of four cylindrical layers arranged concentrically around the beampipe in the barrel region. The innermost layer, known as the Insertable B-Layer (IBL), was installed between Run 1 and Run 2. The pixel detector features a pixel size of 50μm × 400μm (50μm × 250μm for the IBL). Its primary functions include b-tagging, which is the identification of particles containing bottom quarks, and track reconstruction, enabling the precise determination of particle trajectories.

The Semi-Conductor Tracke

The Semi-Conductor Tracker (SCT) is the second component of the inner detector and consists of four layers of silicon microstrips in the barrel region. The SCT plays a crucial role in measuring the momentum of charged particles and determining their vertex location.

Transition Radiation Tracker

The Transition Radiation Tracker: Positioned around the SCT sub-detector, this component comprises numerous layers of 4 mm diameter straw tubes. The TRT serves the purpose of measuring momentum and distinguishing between electrons and hadrons

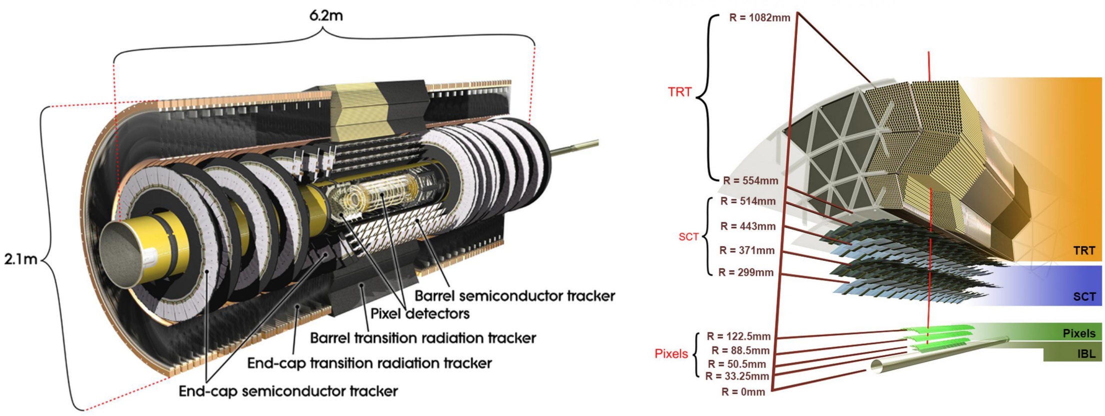

Figure 2.6: Left: An overview of the ATLAS inner detector. Right: Visualization of the ID sensors and structural components crossed by a charged track in the inner barrel detector [42].

2.3.4 Calorimeter system

A calorimetric system is utilized to measure the energy of particles within the region $|\eta| < 4.9$, which is divided into three components (as depicted in the left section of Figure 2.7). The initial component is the electromagnetic liquid argon calorimeter, specifically sensitive to photons and electrons. The second component is the hadronic calorimeter, designed to detect jets. Lastly, the forward calorimeter employs liquid argon to simultaneously detect both hadrons and electrons/photons.

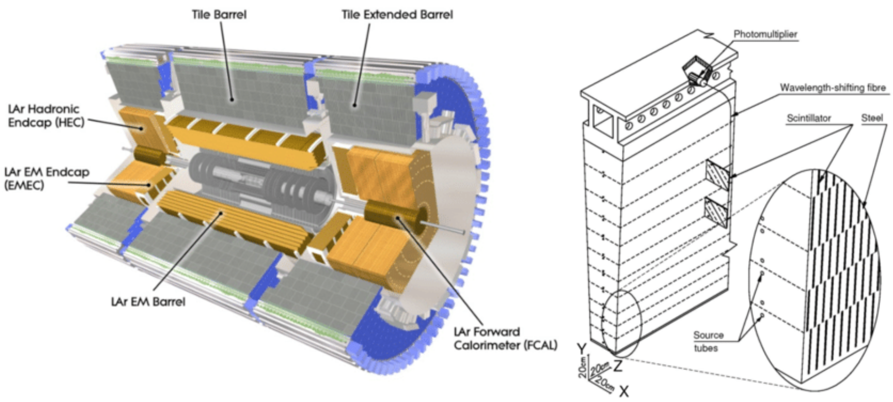

Figure 2.7: (left) ATLAS calorimeter system. (right) Tile calorimeter module internal structure [44].

Electromagnetic liquid argon Calorimeter

The ATLAS experiment utilizes an electromagnetic calorimeter[36, 45] (EM calorimeter), which is a sampling calorimeter designed with alternating layers of lead absorbers and liquid argon active layers. This configuration makes it highly resilient to radiation. It has an accordion-like geometry, which provides very high granularity, complete coverage, and homogeneity along the azimuthal angle φ, as well as fast signal readout. The EM calorimeter is composed of two main parts: the Barrel and the End-caps. The Barrel consists of two half-barrels, separated by a 4mm gap, and it covers the regions $|\eta| < 1.37$. The End-caps are positioned at each end of the Barrel and cover the regions $1.52 < |\eta| < 3.2$. However, the precise measurement region of the End-caps stops at approximately $|\eta| = 2.4$. The region between the Barrel and the End-caps, known as the transition region ($1.37 < \eta < 1.52$), contains a significant amount of inactive material and is not utilized for precise measurements. In the W mass analysis for Run 1, an even larger portion of the detector, specifically $1.2 < \eta < 1.82$, was excluded due to the higher quality wanted and small mismodeling in this region.The EM Calorimeter is divided in three layers : The first layer of the electromagnetic calorimeter has a fine segmentation of $(\Delta\eta \times \Delta\varphi) = (0.0031 \times 0.1)$ to accurately measure the early stages of electromagnetic shower development. In the central region, the second and third layers have coarser segmentations of $(\Delta\eta \times \Delta\varphi) = (0.025 \times 0.025)$ and $(\Delta\eta \times \Delta\varphi) = (0.05 \times 0.025)$, respectively. To correct for energy losses upstream of the EM calorimeter, a pre-sampler is utilized. The pre-sampler is a section of the calorimeter made of liquid argon located before the first layer. Its spatial segmentation is $(\Delta\eta \times \Delta\varphi) = (0.025 \times 0.1)$. The design of the EM calorimeter was optimized for the search of the Higgs boson in the channels $H \to \gamma\gamma$ and $H \to e^+e^-e^+e^-$ of the Standard Model. The energy resolution in both the barrel and endcap sections is provided by the following formula [36]:

$$\frac{\sigma_E}{E} = \frac{10\%}{\sqrt{E}} \oplus 0.7\%$$

In order to account for energy losses occurring before reaching the EM calorimeter, a presampler is employed. The presampler consists of a 1 cm liquid argon active layer in the barrel section and a 5 mm liquid argon active layer in the endcap section. It is equipped with electrodes that are approximately perpendicular to the beam axis in the barrel and parallel to the beam axis in the endcap.

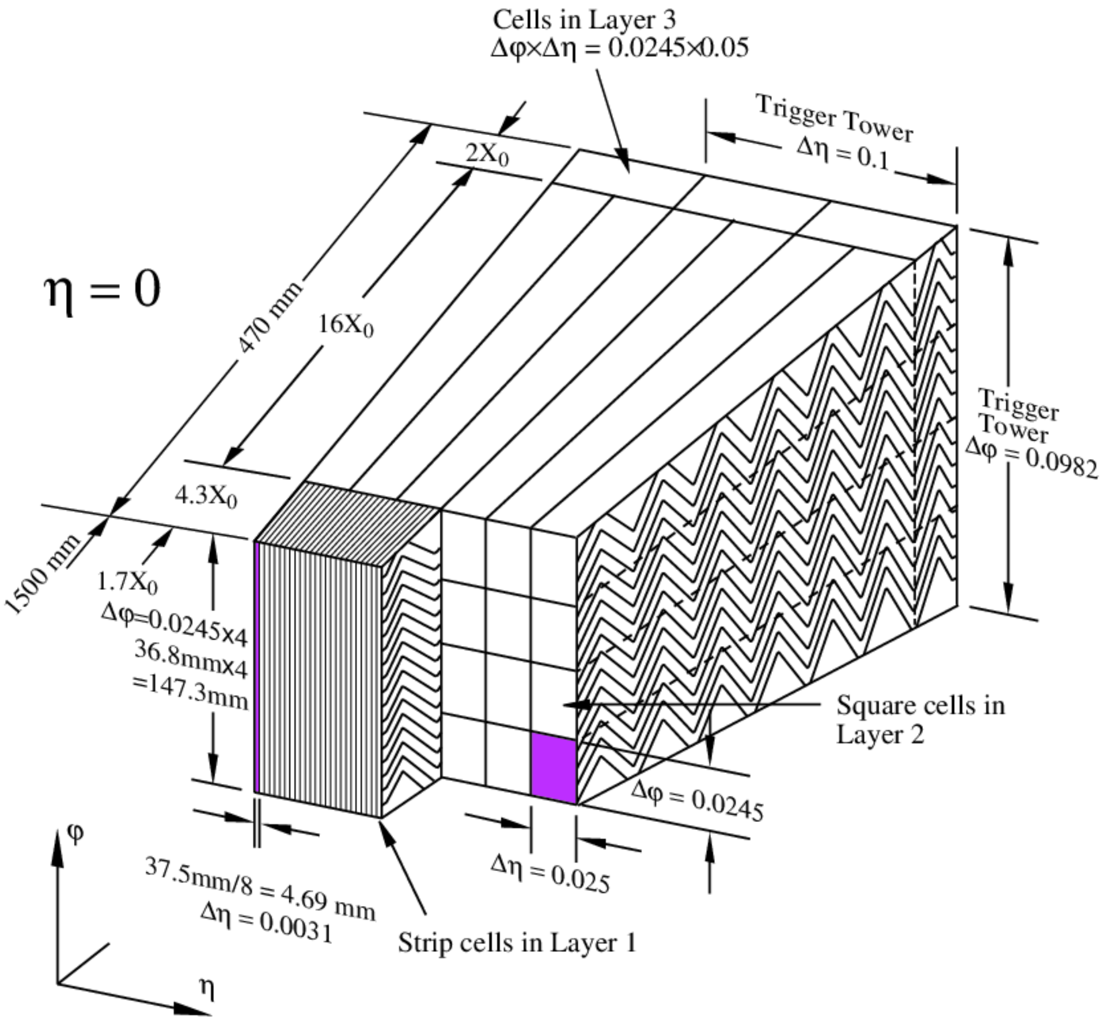

Figure 2.8: Diagram of a LAr EM calorimeter barrel module. It shows the longitudinal segmentation, cell size is shown and the accordion structure [46].

Hadronic Calorimeter

The hadronic calorimeter[36], which complements the electromagnetic calorimeter (ECAL), measures the energy and determines the directions of high-energy hadrons (quarks, gluons) in order to reconstruct jets. Additionally, it plays a role in estimating the missing transverse energy. Positioned behind the EM calorimeter, the tile hadronic calorimeter functions similarly but utilizes iron as the absorber and scintillating tiles as the active material. It consists of three layers that cover the range $|\eta| < 1.7$. The first two layers have an identical granularity of $\Delta\eta \times \Delta\phi = 0.1 \times 0.1$, while the last layer has a granularity of $\Delta\eta \times \Delta\phi = 0.2 \times 0.1$.

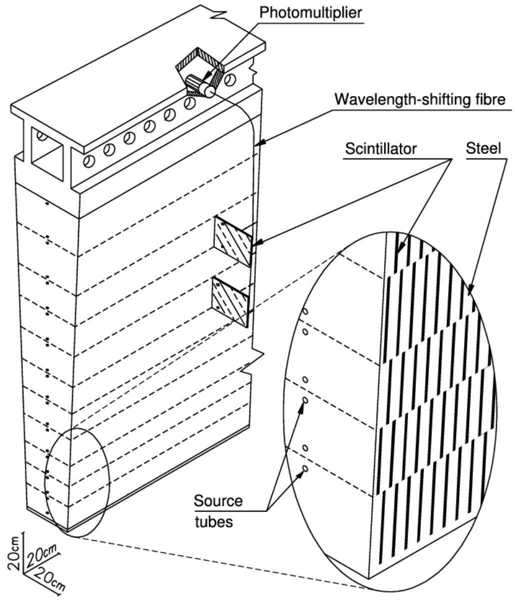

Figure 2.9: Schematic diagram of the ATLAS hadronic tile calorimeter [47].

2.3.5 Muon spectrometer

Like the other sub-detectors mentioned before, the muon spectrometers shown in Figure 2.10 are made up of two parts: a barrel and an end-cap. The end-cap is made specifically to detect muons with higher pseudorapidity values, extending up to $|eta| = 2.7$, while the barrel covers the core areas ($|\eta| < 1$). These components are responsible for determining the curved trajectories of the muons, induced by the magnetic field generated by the toroidal magnet, and measuring their momentum. Each section comprises two types of detectors: a fast-response detector for the triggering system and a precision detector for precise muon measurements, such as pulse and charge. The former includes RPC (Resistive Plate Chambers) and TGC (Thin Gap Chambers) detectors, while the latter consists of MDT (Monitored Drift Tube) and CSC (Cathode Strip Chambers).

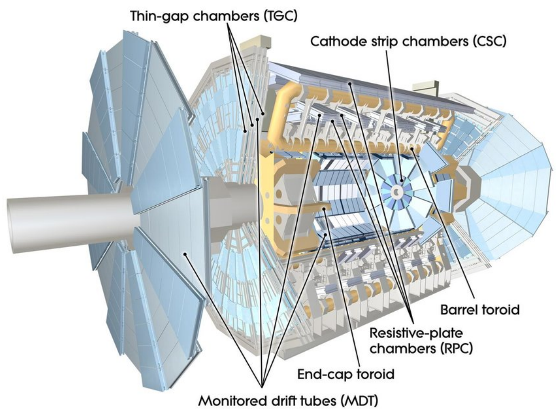

Figure 2.10: Muon spectrometer of the ATLAS detector [48].

2.3.6 ATLAS trigger and data acquisition system

Collisions between proton packets in the ATLAS detector take place at a rate of 25 ns (50 ns in 2012), resulting in an event frequency of 40 MHz (20 MHz in 2012). However, the majority of these events, which involve low energy in the transverse plane or towards the front, are not of significant interest. To handle the processing, reconstruction, and storage of detector information, an event filtering system called the trigger system is implemented[49, 50]. This system, depicted in Figure 2.11, consists of two levels and effectively selects events that are relevant for physics research by utilizing information from the ATLAS sub-detectors. Its primary objective is to selectively identify events that exhibit desired characteristics. From a total of 1 billion events, the trigger system has the capability to select between 100 and 1000 events per second. During Run 2, the trigger system [51] was divided in two parts :

The Level 1 trigger: This is a hardware-based trigger [49] that performs the initial stage of event selection. The L1 trigger utilizes inputs from the muon spectrometer and calorimeter systems to identify signatures such as high-pT muons, electrons/photons, jets, and -lepton decays, aiming to choose the desired events. The L1 trigger reduces the event rate from the LHC bunch crossing rate of 40 MHz to approximately over 100 kHz.

The High-Level Trigger (HLT): Events triggered by the L1 stage are further processed by the HLT to further reduce the event rate to 1 kHz.The HLT reconstructs events using more detailed data, including ID tracks, in order to remove a majority of the pre-selected events[52].

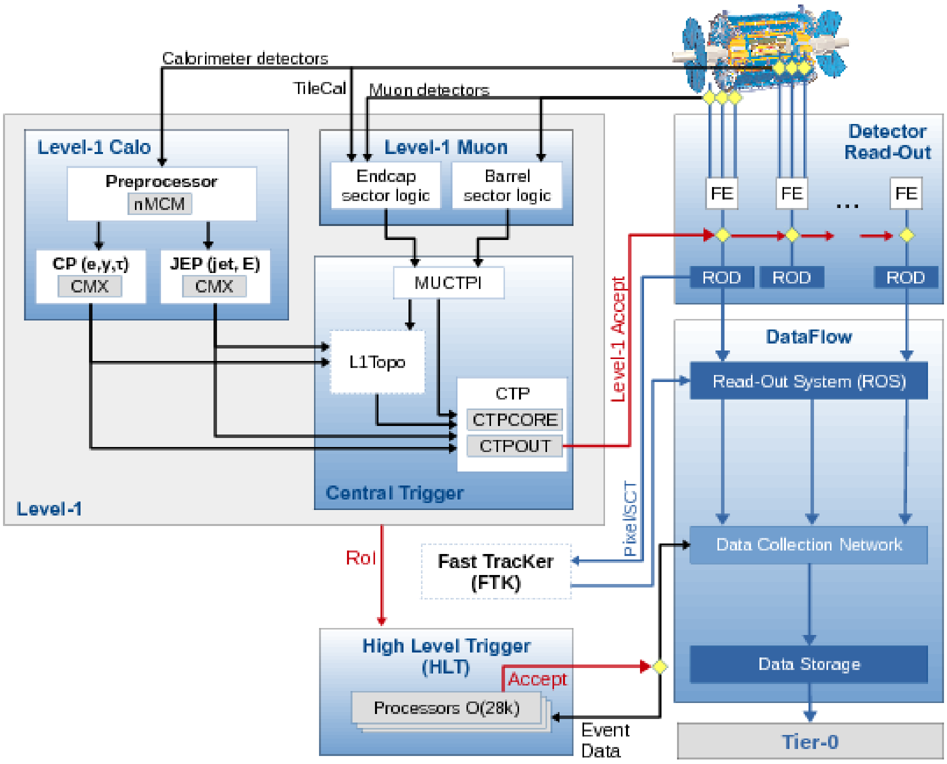

Figure 2.11: An overview of The ATLAS Trigger and Data Acquisition (DAQ) System[52].

2.4 Data, Simulation and Reconstruction of physics objects

2.4.1 Data & Analysis frameworks in ATLAS

Analysis frameworks in ATLAS

The ATLAS collaboration utilizes a software environment called the ATHENA framework[53] for processing, simulating, and reconstructing data. Its primary objective is to manage the extensive range of measurements obtained from the ATLAS detector, deliver processed data objects to physicists, and establish a framework for analyzing the data to generate physical results. ATHENA is built upon the GAUDI software and comprises multiple C++ packages that can be executed using a Python script (jobOptions).

Data

Data acquisition in the ATLAS experiment [54] is organized into runs, each assigned a unique identifier, and further divided into luminosity blocks. These blocks are labeled with data quality information, which is valuable for constructing a "good run list" (GRL) for physics analysis purposes. Subsequently, the collected data is processed using the ATLAS software framework, Athena. The outcome of this processing is the generation of Analysis Object Data (AOD) files, which contain comprehensive information about physics objects, including electrons and muons, along with their properties such as energy, momentum, and position. These AOD files can undergo additional processing to generate Derived Analysis Object Data (DAOD) files, which were utilized in the analysis presented in this study.

2.4.2 Simulation of the ATLAS Detector

In the simulation of the ATLAS detector, the interaction between produced particles and the detector material, as well as the response of the detector electronics, is modeled. The detector geometry is divided into basic volumes representing all parts of the ATLAS detector. The distribution of these volumes is approximately 38% for internal detectors, 32% for calorimeters, and 30% for muon spectrometers[55]. The simulated detector incorporates the real operating conditions recorded in a database.

GEANT4 [56]is the main software used for the complete simulation, providing a detailed description of the detector and physical processes but requiring significant computational time. To speed up calculations, a simplified version called ATLFASTII is available [57][55]. It uses a library of electromagnetic and hadronic showers instead of simulating particle interactions with the detector material [58]. The properties obtained from this simplified simulation are similar to those from the complete simulation, with a small difference in the energy scale of the jets[55].The response of the simulated detector is then converted to match the actual data format, enabling the reconstruction of physical objects such as electrons, muons, jets, and missing transverse energy in both simulated and actual data samples.

2.4.3 Reconstruction of physics objects

The sub-detectors [59] in the ATLAS experiment interact with incident particles based on their properties, allowing for the identification and measurement of their characteristics. Figure 2.12 illustrates that Charged particles like electrons and muons leave traces through ionization in the inner detector. Electrons and photons deposit most of their energy in the electromagnetic calorimeter, while jets, neutrons, and protons are stopped by the hadronic calorimeter. Muons, on the other hand, pass through the calorimeters with minimal energy loss and leave tracks in the muon spectrometer. Neutrinos, however, do not produce detectable signals within the detector.

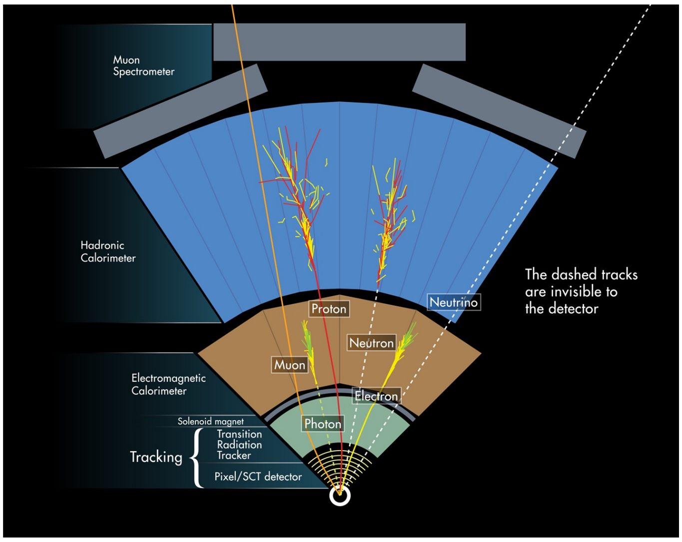

Figure 2.12: Signatures of different types of particles in the subsystems of the ATLAS detector[60].

Muons

In the ATLAS experiment, muons [61] are reconstructed by integrating information from the inner detector and the muon spectrometer through four distinct techniques. These techniques establish four muon classifications: stand-Alone muons (SA), combined muons (CB), segment-tagged muons (ST), and calorimeter-tagged muons (CT).

Stand-Alone reconstruction exclusively employs data from the muon chambers to reconstruct the muon's path, taking into account energy losses in the calorimeters. **Combined** reconstruction merges data from both the inner detector and the muon chambers to generate a final track. **Calorimeter-tagged** reconstruction utilizes a track in the inner detector and energy deposits in the calorimeters, sacrificing muon purity while enhancing acceptance in regions where the muon spectrometer is only partially instrumented, such as around $|\eta| = 0$. **Segment-tagged** reconstruction reconstructs the muon trajectory based on tracks in the inner detector associated with hits in specific detector components(MDT:"Monitored Drift Tubes" or CSC:"Cathode Strip Chambers").

Electrons

Electrons and photons are reconstructed in the EM calorimeter [33] by interacting with lead absorbers, resulting in EM showers. These showers ionize the liquid argon, causing ionization electrons to drift and induce an electric current on the electrode. Due to the longer charge collection time (450 ns) compared to the time between bunch crossings at the LHC, multiple bunch crossings are integrated, leading to significant pileup effects. To address this, the signals undergo bipolar filtering, to make them more peaked and reduce the contribution from pileup.

In the central region ($|\eta| < 2.5$), the reconstruction of electrons and photons follows a new algorithm called superclusters, which replaces the fixed-size cluster approach of the sliding window algorithm [62]. This new algorithm improves the accuracy of electron and photon energy measurement. It begins by **building clusters** of electromagnetic (EM) cells, known as **topo-clusters**:Topo-clusters are created in the EM and hadronic calorimeters by applying noise thresholds. A cell initiating the cluster must have a significance $|S_{\text{cell}}^{\text{EM}}| \geq 4$, where $S_{\text{cell}}^{\text{EM}}$ is the ratio of the cell energy $E_{\text{cell}}^{\text{EM}}$ to the expected cell noise $\sigma_{\text{noise cell}}^{\text{EM}}$. Neighboring cells with energy twice as high as their noise level are iteratively added to the cluster. The resulting topological calorimeter cluster includes cells above their noise level. Electromagnetic topology is selected, and reconstructed tracks and conversion vertices from the inner detector are matched to the electromagnetic using a similar method to the sliding windows algorithm [62].

Additionally, to ensure a significant rejection of pileup and isolate clusters primarily originating from showers in the EM calorimeter, further selections are applied to a topo-cluster. These selections are based on the factor fEM, which is calculated by dividing the sum of energies deposited in the first (E_{L1}), second (E_{L2}), and last ($E_{Cluster}$) layers by the total energy of the cluster (ECluster) [63]:

$$f_{EM} = \frac{E_{L1} + E_{L2} + E_{L3}}{E_{Cluster}}$$

At the end of the selection process, only topo-clusters that satisfy the conditions $f_{EM} > 0.5$ and $E_{Cluster} > 400$ MeV are retained.

In the context of **electron identification** [33], it should be noted that not all electrons reconstructed using the "topological clustering" algorithms are considered prompt electrons (originating directly from the interaction of interest). To distinguish prompt electrons and photons from background objects such as hadronic jets, prompt electrons from photon conversions, and QCD jets, an identification algorithm is employed. This algorithm utilizes a likelihood-based (LH) approach, incorporating information from both the tracking system and the calorimeter system. Its purpose is to accurately select prompt electrons and photons while rejecting background contributions.

Missing transverse momentum

The concept of missing transverse momentum [64] is frequently used in hadron colliders. Since the longitudinal momentum of the initial protons is not precisely known due to the proton's internal structure, momentum conservation is mainly considered in the transverse plane where the protons have no initial momentum. Our analysis includes neutrinos, which are particles that leave the detector without being detected. Therefore, the missing transverse momentum ($\vec{p}_T^{\text{miss}}$) and its magnitude (E_T^{miss}) play a crucial role as they characterize these undetected particles.

The reconstruction of the missing transverse energy involves measuring the energy deposits in the calorimeters and reconstructing muons in the muon spectrometer. Additionally, traces of low-energy particles that do not reach the calorimeters are considered. The expression for E_T^{miss}, is defined as:

$$\begin{aligned} E_{x,y}^{\text{miss}} &= E_{x,y}^{\text{miss,e}} + E_{x,y}^{\text{miss },\mu} + E_{x,y}^{\text{miss, },\tau} + E_{x,y}^{\text{miss, }\gamma} + E_{x,y}^{\text{miss , jets}} + E_{x,y}^{\text{miss, softjet}} \\ E_T^{\text{miss}} &= \sqrt{(E_x^{\text{miss}})^2 + \left(E_y^{\text{miss}}\right)^2} \end{aligned} \tag{2.4}$$

Each term in the expression represents the negative sum of reconstructed objects projected onto the x or y axes.

Hadronic recoil

While the charged leptons produced from the decay of W or Z bosons can be detected by the muon spectrometer or calorimeter, the neutrino escapes the detector without being observed. Therefore, the transverse momentum of the neutrino, denoted as $\vec{p_T}^{\nu}$, is inferred from the missing transverse energy, E_T^{miss} , which can be calculated using the transverse momentum of the charged lepton, $\vec{p_T}^{\ell}$, and the recoil in the transverse plane, $\vec{u}_T$ [64].

The fundamental concept behind the hadronic recoil [65] is to measure the vectorial and scalar sums of all particles resulting from initial state gluon and quark radiation. Since the initial proton-proton collision is balanced in the transverse plane, it directly measures the finite transverse momentum with which the W boson is produced. Additionally, the momentum balance is utilized to determine the transverse momentum of the neutrino. The general relation between these quantities is expressed as:

$$p_T^{\vec{W}} = \vec{p_T}^{\ell} + \vec{p}_T^{\nu} = - \sum_{i=ISRq,g} \vec{p}_{Ti} = -\vec{u}_T \tag{2.5}$$

Here, $p_T^{\vec{W}}$ represents the transverse momentum of the W boson, while $\vec{p_T}^{\ell}$ and $\vec{p}_T^{\nu}$ denote the transverse momenta of the charged decay lepton and the neutrino, respectively. The hadronic recoil, denoted as $-\sum_{i=ISRq,g} p_{Ti} = -u_T$, accounts for the transverse momenta of all partons resulting from initial state radiation and directly measures the transverse momentum of the W boson.

Assuming that uT can be measured, this allows for the indirect determination of the neutrino's transverse momentum, $\vec{p}_T^{\nu}$:

$$E_T^{\vec{miss}} = \vec{p_T}^{\nu} = - \left(\vec{u_T}^{+} \vec{p_T}^{\ell} \right) \tag{2.6}$$

Here, $E_T^{\vec{miss}}$ represents the missing transverse momentum.

The reconstruction of the hadronic recoil [65]involves calculating the vectorial sum of the transverse momenta of all charged and neutral particles in the transverse plane. This recoil $\vec{u}_T$, provides information about the activity and momentum balance of the particles produced in a collision. To characterize the hadronic recoil, additional variables such as $u_\perp$ and $u_\parallel$ are defined (as illustrated in Figure 2.13), which represent the components of the recoil perpendicular and parallel to the transverse momentum vector of the vector boson. The bias is also introduced to account for factors like undetected particles and energy losses. These variables allow for a better understanding of the kinematics and calibration of the hadronic recoil in particle collision events.

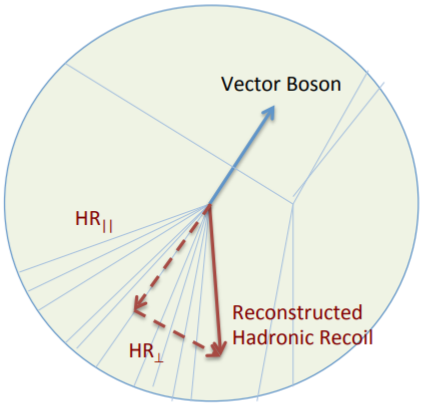

Figure 2.13: Projection of Hadronic Recoil onto Vector Boson: Defining $u_{\|}$ and $u_{\perp}$ Components[66].

Upgrade of ATLAS

After Run 3 [67][68], the LHC will be upgraded to the High-Luminosity LHC (HL-LHC) to increase its data collection rate and achieve higher luminosity. The HL-LHC is expected to start in 2027 with a center of mass energy of 14 TeV and run until at least 2040. It will have an integrated luminosity of 4000 fb^{-1}. The upgrade aims to improve precision measurements of the Standard Model, explore the Higgs sector in more detail, and extend the search for physics beyond the Standard Model.

One significant addition to the upgraded LHC is the High-Granularity Timing Detector (HGTD). The HGTD is designed to provide high-precision time measurements for tracks in the forward region, improving object reconstruction, enhancing pile-up rejection, and enabling reliable luminosity measurements.

2.5 Conclusion

In this chapter, we provide an overview of the experimental setup used for data collection in this thesis. The LHC accelerator complex can accelerate and collide protons and heavy ions at four interaction points. We specifically focus on the ATLAS detector and provide a detailed description of its sub-detectors and their operations. Additionally, we present an overview of the data collection and simulation techniques employed in the ATLAS experiment. Furthermore, we discuss the reconstruction of crucial objects that contribute significantly to determining the mass of the W boson, including electrons, muons, missing transverse energy, and the hadronic recoil.

Chapter 3

W boson mass measurement

3.1 Introduction

This chapter describes the W boson mass measurement using the Run2 data-set recorded by the ATLAS detector, at a center-of-mass energy of $\sqrt{s} = 5\ TeV$, corresponding to 256.827 pb^{-1} of integrated luminosity, The data used are collected using special runs, with low number of interactions per bunch crossing, in order to improve the experimental resolution of the recoil measurement and the reconstruction of the missing transverse momentum and of the transverse mass. In this work, we are interested in the leptonic decays of the W boson, specifically $W^+ \to e^+\nu_e$, and the charged products of this decay, electron or muon, are accompanied by a neutrino. The neutrino can not be measured directly in the detector but can be measured indirectly using the lepton and the hadronic system which recoils against the W boson. Two different approaches are employed: the templates method, which was developed before for the Run 1 analysis [69], and the use of unfolded distributions for our variables of interest. In this chapter, our main focus is on evaluating the statistical uncertainty of the W boson mass measurement using the two aforementioned approaches, and we will discuss the differences between the two methods.

3.2 Data MC samples and W boson selection

3.2.1 DATA

For the purpose of our analysis, which aims to achieve a precise measurement of the W boson mass, we have considered specific runs conducted during Run 2 under low pileup conditions[70]:

- The data used was obtained from proton-proton collisions at a center-of-mass energy of $\sqrt{s} = 5.02$ TeV
- The data was collected in November 2017, with an integrated luminosity of 256.827 pb^{-1}
- ATLAS data period M
- GRL data17_5TeV.periodAllYear_DetStatus-v98-pro21-16_Unknown_PHYS_ StandardGRL_All_Good_ignore_GLOBAL_LOWMU.xml;
- Runs 340644, 340683, 340697, 340718, 340814, 340849, 340850, 340910, 340925, 340973, 341027,341123, 341184;

- The data was collected over a range of interactions per bunch crossing, denoted by $\langle\mu\rangle$, starting at approximately $\langle\mu\rangle \sim 5$ and decreasing throughout the run to around $\langle\mu\rangle \sim 1$.

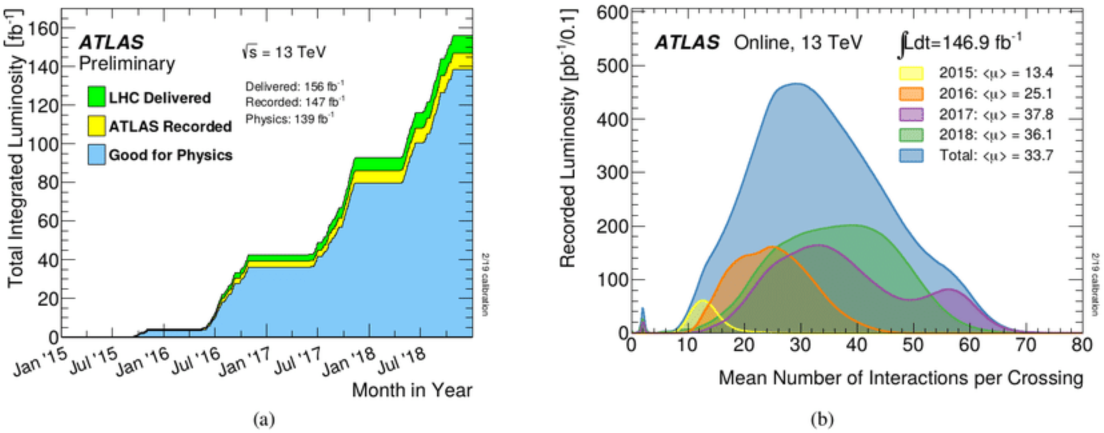

Figure 3.1: (left) Total integrated luminosity collected by ATLAS in Run-2. (right): recorded luminosity as a function of the number of interactions per crossing in each year of Run-2

3.2.2 MC samples

For this analysis, the MC samples[70] were generated using the POWHEG event generator with the CT10 PDF interfaced to PYTHIA8. Additionally, the Powheg+Pythia8 samples are interfaced with Photos++ to account for the effects of QED radiation in the final state. Theoretical calculations are performed at the NNLO (Next-to-Next-to-Leading Order) using PDF sets that describe the distribution of partons within the protons. In this study, the CT18 PDF set is used as a reference.The masse of the W boson was assumed to be MW = 80399 MeV for the nominal simulations.

All the simulated samples were processed through the GEANT4 based simulation of the ATLAS detector. The events were then reconstructed using the ATLAS software framework, following the same analysis chain as data.

3.2.3 W boson selection

In order to minimize the background effects and increase the resolution, a set of selection criteria is applied[70]:

- events are required to contain one lepton with a transverse momentum $p_T^l > 25GeV$
- missing transverse energy $E_T^{miss} > 25GeV$
- transverse mass of W boson which is defined as $m_T^W = \sqrt{2p_T^\ell p_T^{miss}(1-\cos(\Delta\phi))}$, where $\Delta\phi$ is the azimuthal opening angle between the charged lepton and the missing transverse momentum, is required to be $m_T^W > 50GeV$

The selection criteria have been carefully optimized to diminish the impact of the multi-jet background and to minimize uncertainties in the measurement of the W boson mass.

3.3 Methodology

As mentioned in section in section 1.3.2, the W boson is an unstable particle that decays into either jets or a lepton-neutrino pair. Measuring jets [66] accurately is challenging due to the energy resolution of reconstructed jets being affected by the significant hadron activity at hadron colliders. On the other hand, energetic leptons can be reconstructed with high precision, making the lepton channel a practical choice for studying the W boson.

As discussed in section 2.4.3, one of the decay products of the W boson, the neutrino, leaves the detector undetected, making invariant mass reconstruction impossible. Nevertheless, it is possible to determine the magnitude and direction of the neutrino's momentum in the transverse plane, denoted as $\vec{p}_T^{\nu}$, from the momentum imbalance of the visible particles in an event, $\vec{p}_T^{\nu}$ is inferred from the vector of the missing transverse momentum, $\vec{p}_T^{\text{miss}}$ (corresponds to the momentum imbalance in the transverse plane) and is defined as :

$$\vec{p}_T^{\text{miss}} = -\left(\vec{p}_T^{\ell} + \vec{u}_T\right) \tag{3.1}$$

Where $\vec{U}_T$, represents the recoil in the transverse plane which is equal to the sum of the transverse energy of all clusters reconstructed in the calorimeters excluding energy deposits associated with the decay leptons : $\vec{U}_T = \Sigma \vec{E}_{T,i}$. Consequently, all kinematic variables are considered in the transverse plane. While it is not possible to directly reconstruct the invariant mass of the W boson, the transverse distributions of its decay products contain sufficient information for extracting the W boson mass.The most important observables, which are sensitive to the W-boson mass [66][26]:

- Transverse momentum of the charged lepton p_T^l
- Missing transverse energy $E_T^{\text{miss}} = p_T^{\nu}$
- Transverse mass of the W boson $m_T^W = \sqrt{2 p_T^{\ell} E_T^{\text{miss}} \left(1 - \cos\left(p_T^{\ell}, E_T^{\text{miss}}\right)\right)}$

The missing transverse energy (E_T^{miss}) will not be used due to the poor experimental resolution of the recoil measurement. The determination of the W boson mass relies on the distributions of the transverse mass of W m_T^W and the transverse momentum of the charged lepton p_T^l. It exploits the kinematic peaks of these distributions.The transverse momentum distribution has a Jacobian peak at $p_T = \frac{m_W}{2}$, whereas the transverse mass spectrum peaks at $m_T^W = m_W$ [64].

Figure 3.2 displays the distributions of p_T^e and m_T^W, without including the background contribution. Additionally, Figure 3.3 provides evidence that the peaks in the distribution of m_T^W are centered around the value of m_W. Similarly, the distribution of p_T^e exhibits peaks around $m_W/2$, which aligns with the expected kinematic properties of the W boson decay. In Figure 3.3, the lower panel is dedicated to displaying the ratio of data over Monte Carlo (MC), allowing for a comparison between the observed data and the simulated Monte Carlo events.

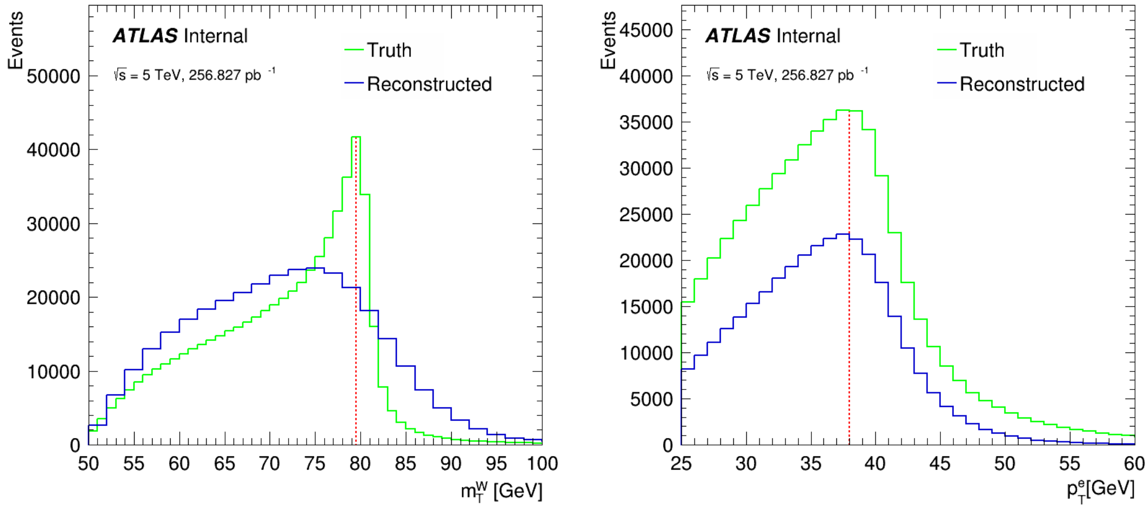

Figure 3.2: The spectra of m_T^W (left) and p_T^e (right) in the electron channel at the truth level and accounting for detector effects (The red line represents the Jacobian peak).

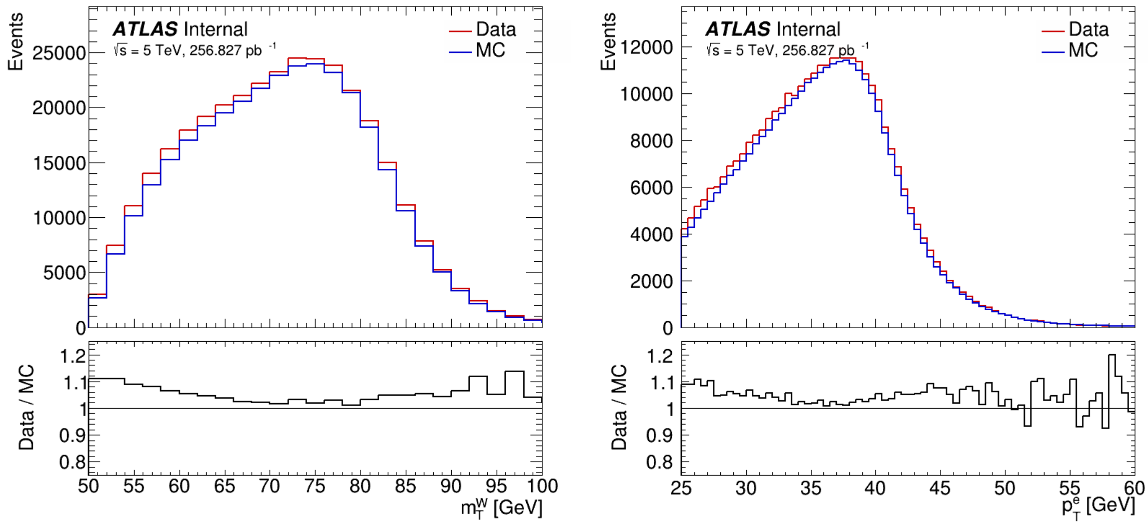

Figure 3.3: Data versus MC distribution for m_T^W (left) and p_T^e(right)

The fundamental concept of the template method [66] is to calculate the distributions of p_T^l and m_T^W for various assumed values of m_W, referred to as templates. By comparing the simulated distributions for different m_W hypotheses with the DATA, the minimal residual difference can be used to determine the actual mass of the W boson.This basic principle is illustrated in Figure 3.4,which represents a comparison between the distributions of p_T^e and m_T^W, and the corresponding templates generated using various mass values, additionally, it can be observed that the various distributions exhibit a common peak.

To minimise the computing time, the templates with different W masses [26] are created by reweighting the truth level distributions using the Breit-Wigner equation :

$$\frac{d\sigma}{dm} \propto \frac{m^2}{\left(m^2 - m_W^2\right)^2 + \frac{m^4 \Gamma_W^2}{m_W^2}} \tag{3.2}$$

where m is the invariant mass of the vector-boson decay products, m_W and Γ_W are the mass and width of the W boson respectively : $\Gamma_W = \frac{\hbar}{2 \cdot m_W} \sqrt{2} \cdot G_F \cdot \frac{m_W^3}{12\pi}$ Due to the large statistics required, the simulation is performed using a single mass value, namely m_W = 80.399 GeV. The weight applied to the truth distributions is regarded as follows:

$$\text{weight} = \frac{f(m'_W)}{f(m_W)} \tag{3.3}$$

with m'_W is the modified mass.

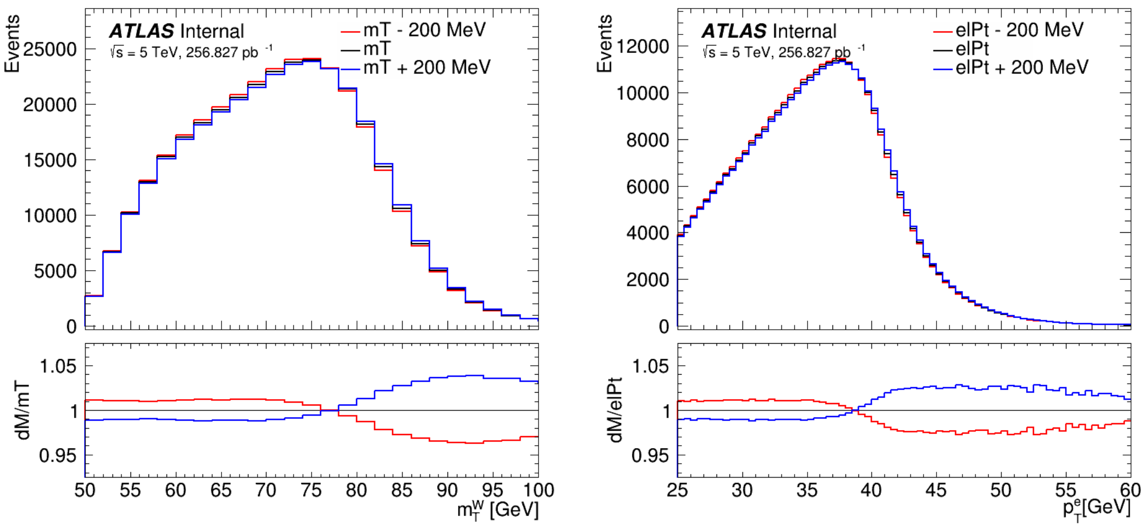

Figure 3.4: m_T^W (left) and p_T^e (right) distributions in simulated events for the W boson mass nominal value m_W = 80399 MeV and the shifted values m_W = 80199 MeV and MW = 80599 MeV. The lower panel illustrates the ratio of the mass variations compared to the nominal mass template.

3.4 Measurement strategy

The W boson mass measurement involves the comparison between the data and a set of templates of the aforementioned observables. In this study, we will utilize the m_T^W and p_T^e distributions.

The comparison between the data and the templates is established using the χ^2 test, which is defined as follows:

$$\chi^2 = \sum_{i=1}^{N} \frac{\left(n_i^{\text{data}} - n_i^{\text{template}}\right)^2}{\left(\sigma_{n_i}^{\text{data}}\right)^2 + \left(\sigma_{n_i}^{\text{template}}\right)^2} \tag{3.4}$$

where :

- $n_{1,i}(f_{2,i})$ is the number of entries in bin i of data (template);

- $\sigma_{n_{1,i}}(\sigma_{f_{2,i}})$ is the uncertainty in bin i of data (template).

First, the χ^2 is calculated between the data and each template individually, resulting in a list of 11 χ^2 values for each observable. These χ^2 values are then fitted using a polynomial function:

$$\chi^2 \approx \chi^2_{\text{min}} + \left(M_W^{temp} - M_W\right)^2 \tag{3.5}$$

where:

-χ^2_{min} refers to the minimum value of the χ^2 distribution;

-M_W represents the measured mass value of the W boson where the minimum is achieved.

The minimum of the χ^2 distribution provides the optimal m_W value.The templates utilized in the W-mass fit are signal Monte Carlo (MC) samples that have been reweighted to m_W ± [0, 25, 50, 100, 150, 200] MeV. Figure 3.5 illustrates the fitted χ^2 distribution for our variables of interest.

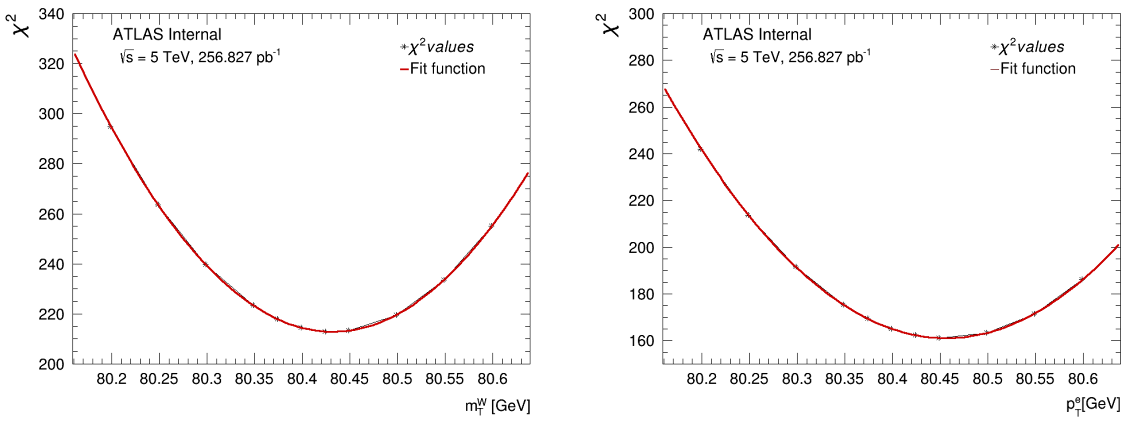

Figure 3.5: Fitting the χ^2 distribution, m_T^W (left) and p_T^e (right), with a parabola (red line) at different template mass values (11 templates). The minimum of the χ^2 corresponds to the extracted mass value.

Note: To verify the effectiveness of the template method, the chi-square test is applied between the signal MC sample with a central m_W of 80.399 GeV and the 11 templates. The same procedure as described above is then followed. Figure 3.6 demonstrates the consistency of our approach for both observables, m_T^W and p_T^e.

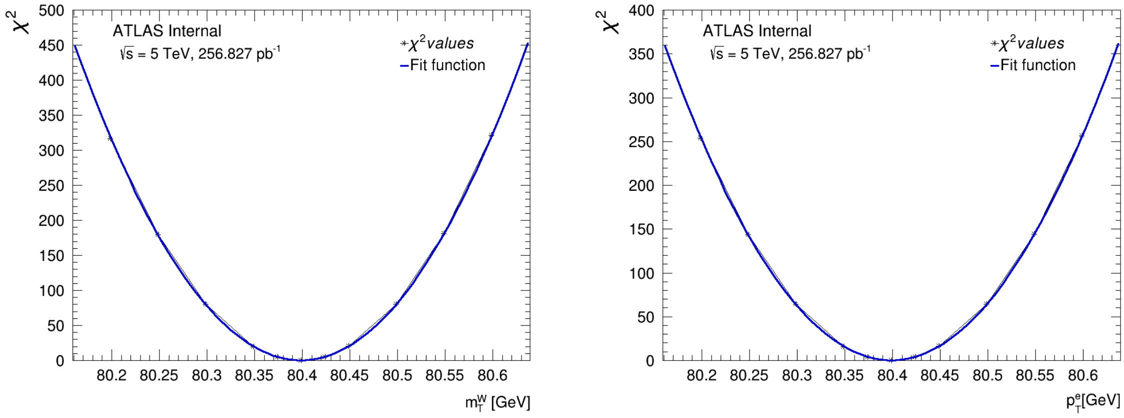

Figure 3.6: Consistency test of the template method for m_T^W (left) and p_T^e (right). The minimum of the χ^2 corresponds to the extracted mass value, which is equal to the nominal value $m_W = 80.399$ GeV.

Statistical uncertainty: The statistical uncertainty is estimated by measuring the width of the parabola described by Equation 3.5, and corresponds to deviation from measured M_W to M_W^{temp} with $\chi^2_{\min+1}$. The following table summarizes the extracted values of m_W from the two distributions, p_T^e and m_T^W, along with their statistical uncertainties.

	$m_{\mathrm{T}}^{\mathrm{W}} \pm \sigma_{stat}$	$p_{\mathrm{T}}^{e} \pm \sigma_{stat}$
MC	80.398 ± 0.011	80.398 ± 0.012
DATA	80.431 ± 0.025	80.456 ± 0.028

Table 3.1: The values of the W boson mass, along with their corresponding statistical uncertainties, for the two observables m_T^W and p_T^e, expressed in GeV.The first row of the table represents the extracted W mass value and the expected statistical uncertainty in the consistency test of the template fit method.

3.5 Correlations between W boson observables

Given that the W boson mass can be extracted from m_T^W and p_T^e distributions, it is important to consider the correlation between these two variables.In this study, the correlation is determined by utilizing Monte Carlo (MC) simulations. A total of 400 MC toys are generated by simultaneously varying the p_T^e and m_T^W distributions with a random Poisson variation. For each toy, the W boson mass is then calculated.

Bootstrapping: In this study, a total of 400 toys are generated using the bootstrap method, whose basic principle consists of sampling with replacement, this Monte Carlo Simulation approach is a convenient method that avoids the cost of repeating the experiment to get other groups of sample data [71]. Bootstrap resampling, combined with a random Poisson variation, is employed to create these toys.

In this study, the template method described in section 3.33.4 is applied to each toy sample along with the 11 templates. This process results in 400 lists of chi-squared values, each containing 11 values. The next step involves fitting the distribution of chi-squared values, and the minimum of each curve corresponds to the extracted mass of the W boson. As a result, we obtain 400 W boson mass values for both the m_T^W and p_T^e observables. This procedure is applied for different η regions,as defined in Table. Finally, we plot the correlation between the two distributions, where the x-axis represents the W boson mass extracted from the p_T^e distribution, and the y-axis represents the W boson mass obtained from the m_T^W distribution.Figure B.8 shows an example of the correlation between p_T^l and m_T^W with the corresponding correlation factor for different ranges of $|\eta|$.

The correlation factor is calculated using the following formula:

$$r = \frac{\sum_{i=1}^{N}(X_i - \bar{X})(Y_i - \bar{Y})}{\sqrt{\sum_{i=1}^{N}(X_i - \bar{X})^2}\sqrt{\sum_{i=1}^{N}(Y_i - \bar{Y})^2}} \tag{3.6}$$

where :
N is the number of toys;
Xi (Yi) represent the W mass results for toy i of p_T^e (m_T^W);
$\bar{X}$ ($\bar{Y}$) is the average of all the measured values X_i (Y_i).

Decay channel	$W \to e\nu$
Kinematic distributions	m_T^W,p_T^e
Charge categories	W^+
$\lvert\eta\rvert$ categories	[0,0.6], [0.6,1.2], [1.8,2.4]

Table 3.2: Summary of categories and kinematic distributions utilized in the analysis of W boson mass for the electron channel[26].

Combination Procedure and Correlations

Statistical uncertainty :

The statistical uncertainties are determined using the distributions of p_T^e and m_T^W separately, and subsequently combining them to obtain the final uncertainty estimate.

In this research to estimate the statistical uncertainties, we utilize the correlation results obtained from the analysis conducted in Section 3.5. Furthermore, We consider the statistical uncertainties calculated for both the p_T^e and m_T^W distributions in different $|\eta|$ regions,Figures 3.8 and 3.9 present the template approach applied to the p_T^e and m_T^W distributions for different $|\eta|$ regions.Finally, we calculate the combined statistical uncertainty between the two observables. The summary of these calculations can be found in Table 3.3.

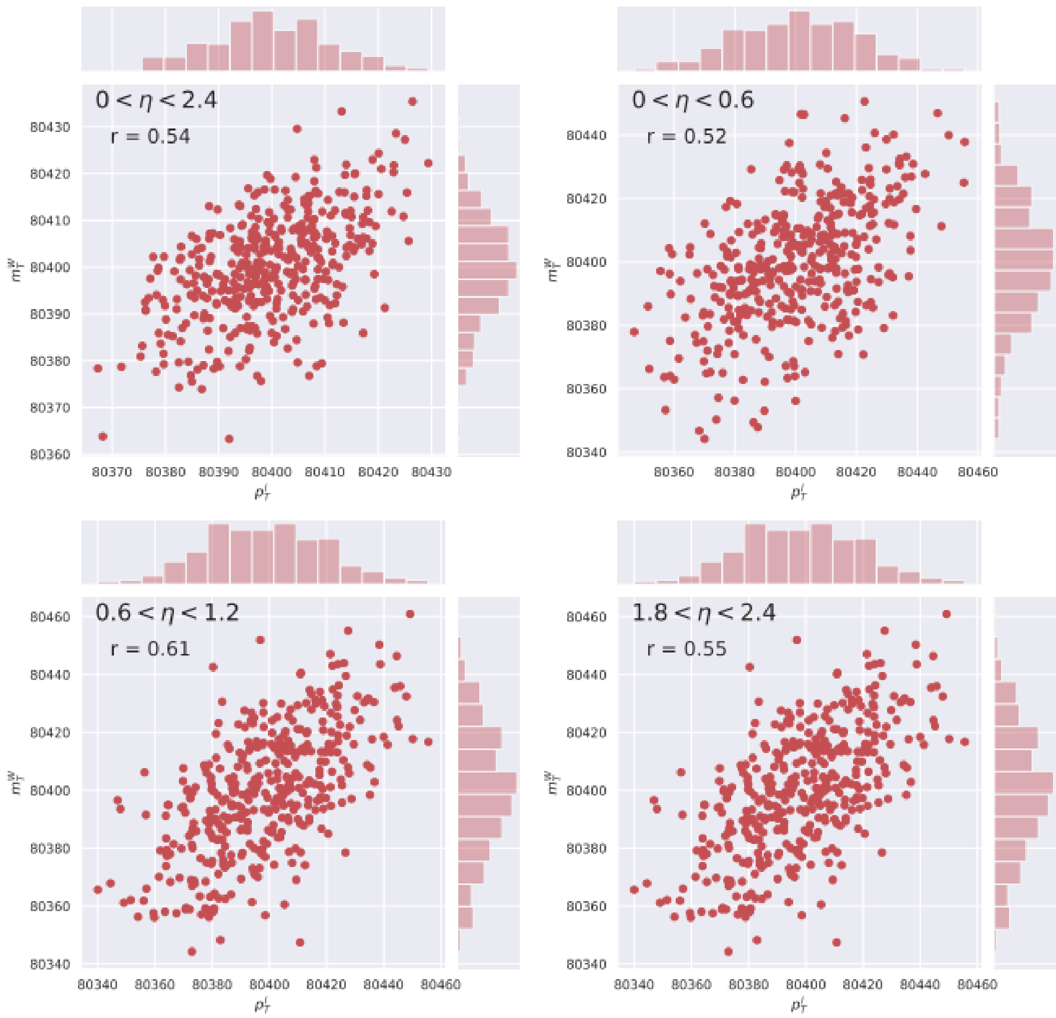

Figure 3.7: Correlation between p_T^l and m_T^W with the corresponding correlation factor for different ranges of $|\eta|$ [33].

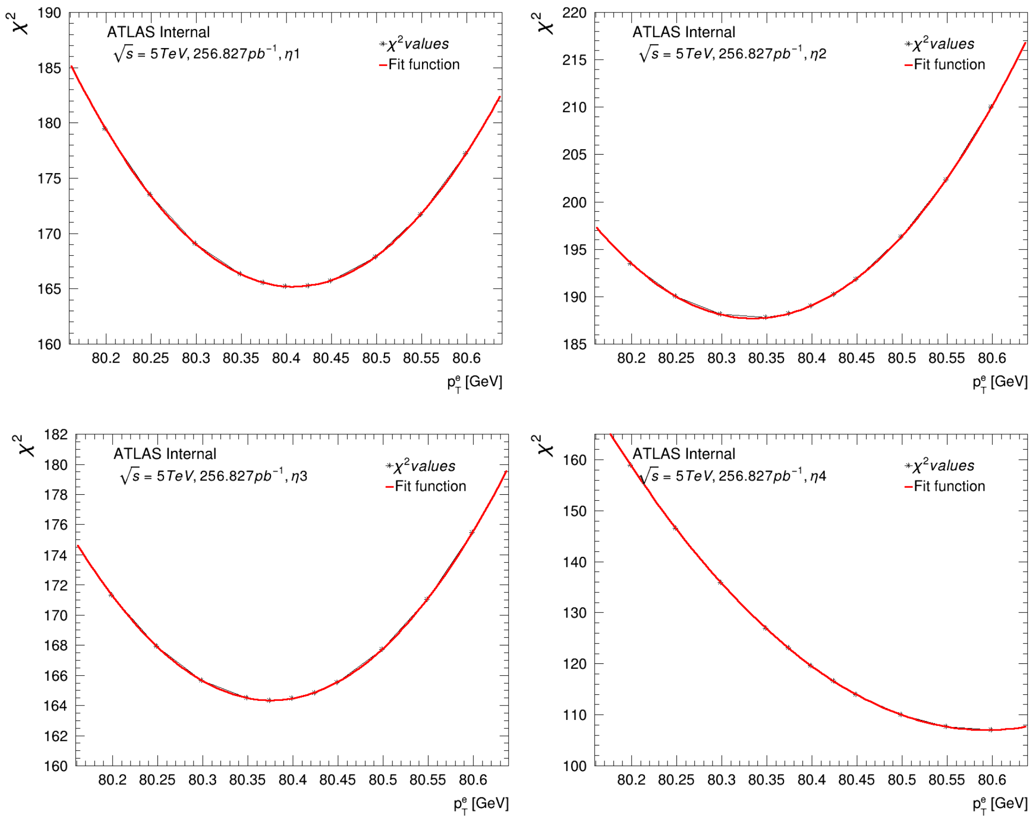

Figure 3.8: Fit to χ^2 distribution at different template mass values for different η regions-p_T^e observable.

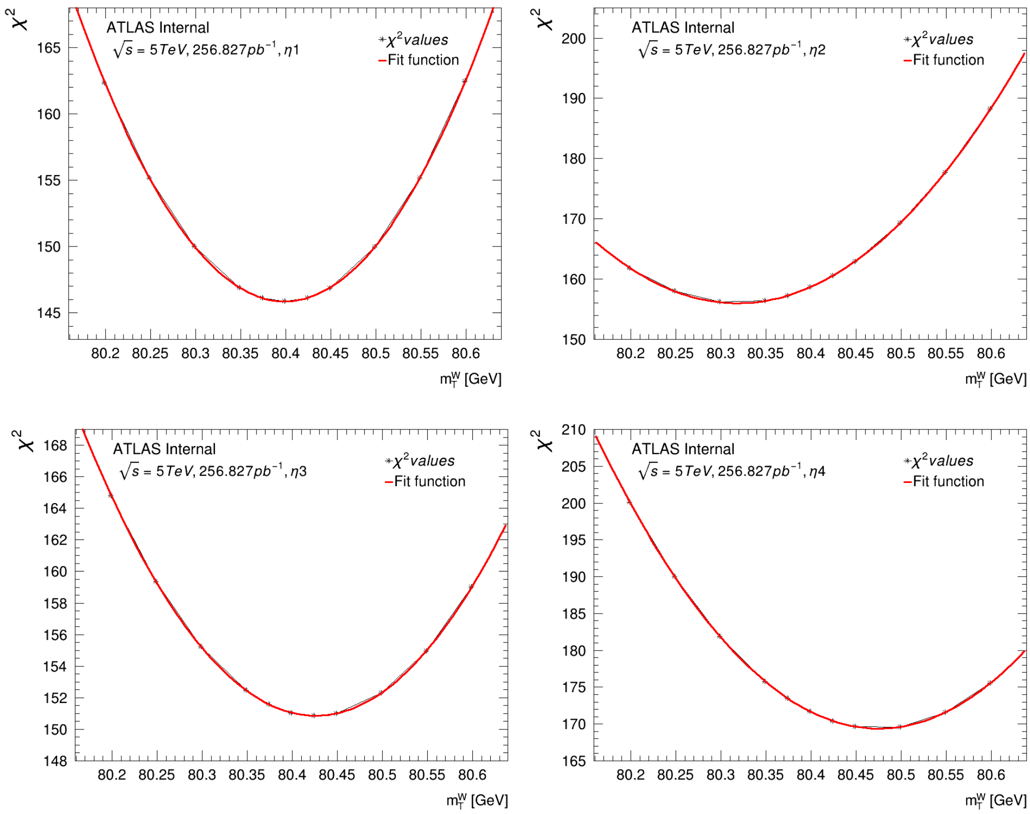

Figure 3.9: Fit to χ^2 distribution at different template mass values for different η regions-m_T^W observable.

η_l **range**	**[0,0.6]**	**[0.6,1.2]**	**[1.2,1.8]**	**[1.8,2.4]**	**[0,2.4]**
Kinematic distribution	p_T^l m_T^W	p_T^l m_T^W	p_T^l m_T^W	p_T^l m_T^W	p_T^l m_T^W
Channel		$W^+ \to e^+\nu_e$, 5TeV			
Stat[MeV]	55 49	56 49	66 60	54 49	28 25
Correlation	0.57	0.60	0.59	0.57	0.56
Combined	46	46.5	55.8	45.6	23.4

Table 3.3: Statistical uncertainties in the m_W measurement for the different kinematic distributions and their combination in different $|\eta_l|$ regions using data sets of 5 TeV.

where: combined=$\frac{1}{2}\sqrt{(\sigma_{p_T^e})^2.(\sigma_{m_T^W})^2 + (2.r.\sigma_{p_T^e}\sigma_{m_T^W}.)}$

3.6 Measurement of W boson mass using Unfolding

In addition to the previously described method, an alternative approach involves utilizing distributions at the unfolded level rather than the reconstructed level. The fundamental concept is to utilize distributions that have already been corrected by the unfolding procedure, eliminating any undesirable detector effects[72]. In this section, we will discuss the theoretical aspects of the unfolding problem and its application to the measurement of the mass of the W boson.

3.6.1 Unfolding in high energy physics

In the field of high energy physics, our focus lies in examining the distributions of the observables of interest. However, these distributions are often affected by detector effects of varying magnitudes. The reconstructed distributions differ from the true distributions due to two primary factors[73]:

- Limited acceptance: This reflects the fact that not all events are detectable by the detector.
- Migration: Due to the finite resolution of the detector, an event originating from one bin (i) can be measured in a different bin (j). To account for this effect, we employ a migration matrix, which we will discuss in detail later on.

In our case, we are particularly interested in the distributions of the transverse momentum p_T^e and transverse mass of the W boson m_T^W. It is worth noting that the m_T^W is more influenced by detector effects compared to the p_T^e, primarily due to the impact of recoil. To obtain results that are independent of these detector and reconstruction effects, we employ the unfolding technique, whose primary objective is to correct data distributions and estimate the true physical distributions of the observables of interest, eliminating any influence from detector effects. As a result, the unfolding results can be directly compared to theoretical predictions or other experiments, in our specific case, they will be utilized for precision measurements of the W boson mass.

To provide a mathematical explanation of the unfolding problem[74][33], let's assume that we have MC simulation vectors x (y) with dimensions $N_x(N_y)$. These vectors represent the number of events in bin i in our distribution at the truth (reconstructed) level, where $x_i(y_i)$ corresponds to each element. Introducing the response matrix R, the relationship between x and y is established. The element $R_{i,j}$ of the response matrix[75] represents the conditional probability P(i|j) for an event generated in truth-level bin j to be reconstructed in reco-level bin i:

$$R \times x = y \tag{3.7}$$

In practice, in real scenarios, the response matrix R is derived from the migration matrix M, whose elements $M_{i,j}$ represent[75] the joint probability P(j,i) for an event to be produced in truth level bin j and reconstructed in reco-level bin i. These values $M_{i,j}$ are estimated using information obtained from MC simulation, by constructing a two-dimensional histogram that includes all selected events. This histogram is filled based on a common matching of the truth and reconstructed values:

$$M_{i,j} = N_{i,j}^{rec \wedge \text{ gen}} \tag{3.8}$$

In this context, $N_{i,j}^{rec\wedge \text{ gen}}$ represents the number of event generated in truth bin j and reconstructed in bin i. The response matrix subsequently defined as follows:

$$R_{i,j} = \frac{M_{i,j}}{N_j^{\text{gen}}} \tag{3.9}$$

where N_j^{gen} represents the number of event generated in truth bin j.

Now, let's consider the case of real data, where we lack any knowledge about the distributions at the truth level. In this case, the concept of unfolding involves applying the inverse of the response matrix, which is calculated using MC simulation, to the real data in order to estimate the true physical distributions. At this stage, the unfolding problem transforms into an inversion problem of the response matrix[33] :

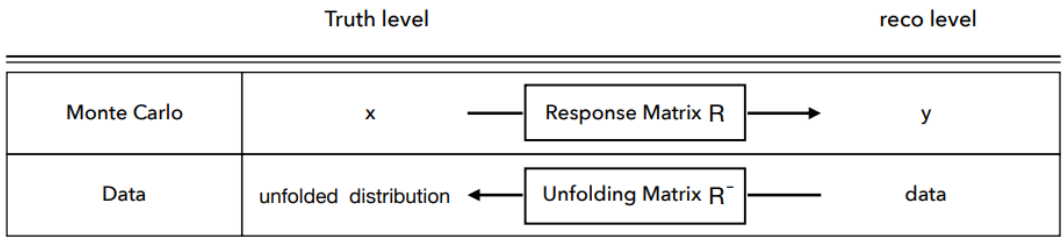

3.6.2 Iterative Bayesian unfolding

In this work, the unfolding of our variables of interest is performed using RooUnfold[76], which is a framework specifically designed for unfolding in ROOT. RooUnfold offers a range of unfolding methods, and in our study, we focus on the Iterative Bayesian unfolding method proposed by D'Agostini.
The iterative Bayesian unfolding method[77] is rooted in Bayes theorem, which provides a framework for calculating the probability of an effect based on prior knowledge of its causes. In our case, we consider a set of causes (C) and effects (E), where causes represent the true values and effects represent the values after smearing. Each effect is influenced by multiple causes. The main objective of unfolding is to estimate the probability $P(C_i|E_j)$, which corresponds to the chance of observing a cause Ci that is responsible for the observed effects E_j. In essence, we aim to determine the probability of attributing the observed effects to a specific underlying cause. In the context of Bayes' theorem, the probability $P(C_i|E_j)$ can be computed as follows:

$$P\left(C_i \mid E_j\right) = \frac{P\left(E_j \mid C_i\right) \cdot P\left(C_i\right)}{\sum_{l=1}^{n_C} P\left(E_j \mid C_l\right) \cdot P\left(C_l\right)} \tag{3.10}$$

The value of n_c represents the number of possible causes, $P(E_j|C_i)$ denotes the probability of observing the effect E_j knowing the cause C_i, and $P(C_i)$ represents the probability of observing the cause C_i. response matrix :

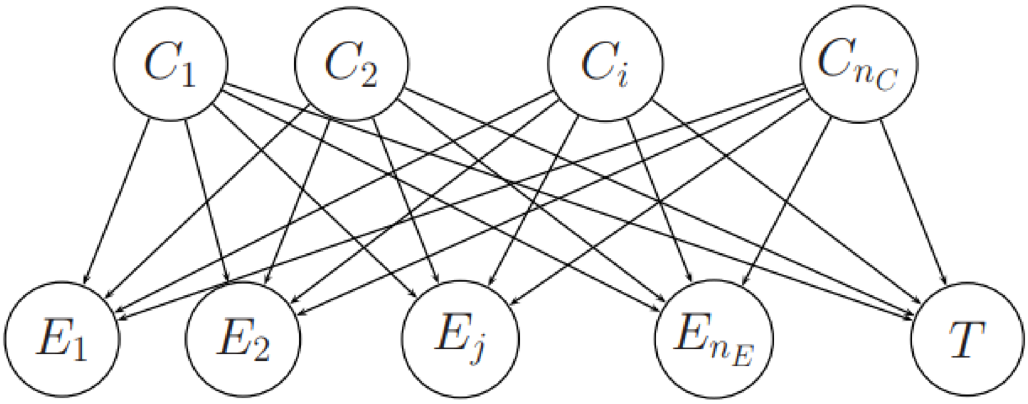

Figure 3.10: Probabilistic connections between causes and effects. The node T represents events that were not detected[77].

The iterative Bayesian unfolding method incorporates a certain level of bias introduced during the unfolding process, which is considered as a source of uncertainty. However, as the number of iterations increases, this bias tends to decrease. To mitigate the unfolding bias, a regularization parameter is employed. The regularization approach involves performing multiple repetitions of the unfolding procedure.

3.6.3 Testing unfolding results: Closure test

Response matrix

In our analysis, we possess the migration matrix that contains information from the truth and reconstructed levels, The migration matrix is determined using the simulation samples, Powheg+Pythia8. By utilizing the RooUnfoldResponse class, integrated within RooUnfold, we generate the response matrix from our migration matrix.The RooUnfoldResponse class contains the measured and truth distributions as TH1s, and the response matrix as a TH2. Additionally, it provides methods for handling these data.To visualize the response matrix, we employ the HresponseNoOverflow method. Figure 3.11presents an illustrative example of the response matrix for the p_T^e and the m_T^W variables, where the x-axis corresponds to reconstructed bins and the y-axis corresponds to truth bins. The figure clearly shows that the transverse mass m_T^W is characterized by a larger migration between the truth and reconstructed levels due to the detector effects. These effects have a stronger impact on the m_T^W compared to the p_T^e.

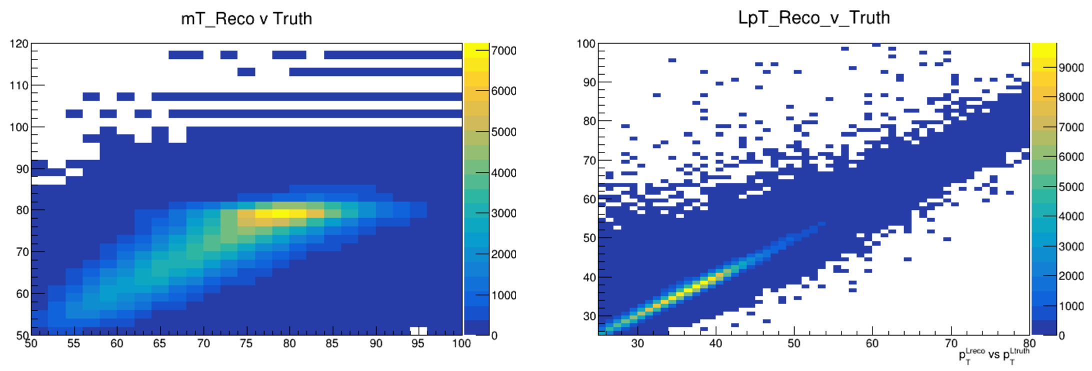

Figure 3.11: Example of the response matrix for p_T^e (right) and m_T^W (left).

In addition to the migration and response matrix, two important factors are applied before and after the unfolding process[33] :

- The first factor is **the efficiency correction**, which is defined as the ratio of events that pass both the reconstructed and truth level selections ($N^{\text{reco,truth}}$) to the number of events that meet the selection criteria at the reconstruction level (N^{reco}). This correction, denoted as ϵ_i, is a function of the reconstructed bin number (i). It is applied before unfolding in order to correct the data distributions, as the data events only pass the reconstructed selections.

$$\epsilon_i = \frac{N^{\text{reco,truth}}}{N^{\text{reco}}}. \tag{3.11}$$

- The second factor is **the acceptance correction**, which is defined as the ratio of events that pass both the reconstructed and truth level selections ($N^{\text{reco,truth}}$) to the number of events that meet the selection criteria at the truth level (N^{truth}). This correction, denoted as A_i, is a function of the truth bin number (i). The inverse of the acceptance correction is applied to the unfolded distribution to extrapolate to the truth fiducial phase space. This step is necessary because the unfolding process is performed using a response matrix that is obtained with events satisfying both the truth and reconstructed criteria.

$$A_i = \frac{N^{\text{reco,truth}}}{N^{\text{truth}}} \tag{3.12}$$

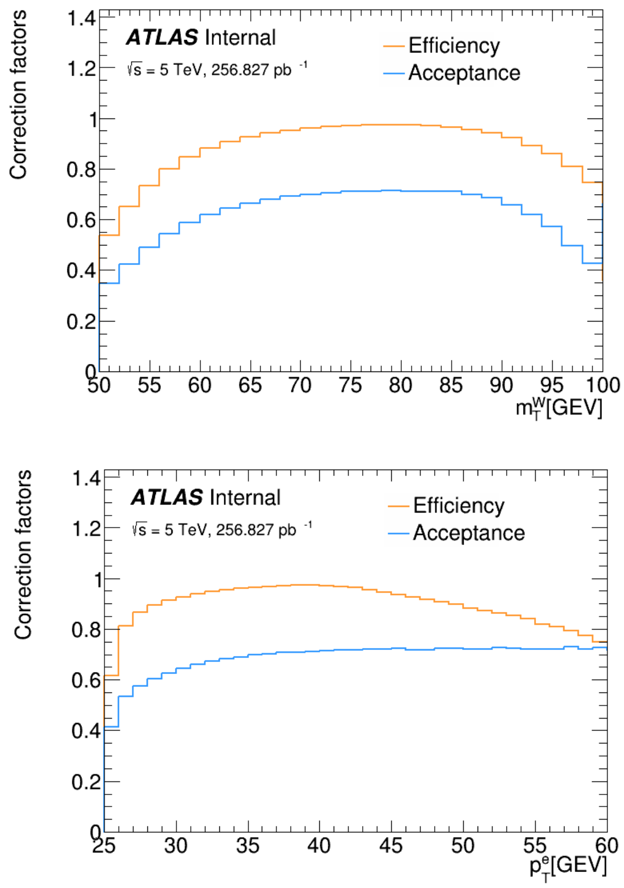

Figure 3.12: An illustration of the acceptance and efficiency factors for the observables m_T^W and p_T^e.

Closure Test

A closure test[74] is a procedure used to assess the performance of a method or technique, specifically, in our case, to verify the reliability of the unfolding method and its ability to recover the true distributions of the observables of interest. In the context of the mentioned unfolding, the closure test involves applying the inverse of the migration matrix to the reconstructed simulation distribution. By doing so, we obtain an estimation of the true physical distributions by correcting for the effects of migration. This test serves as a validation step to ensure the accuracy of the unfolding process and its capability to recover the underlying truth distributions.

In the context of the closure test conducted in this section, our objective is to apply unfolding to the observables p_T^e and m_T^W using the RooUnfold package. We apply the efficiency correction to the reconstructed simulation distribution, and the acceptance correction is applied to the unfolded distribution. To obtain the results, we employ the RooUnfoldBayes class, which incorporates the Bayesian unfolding technique. The unfolding result is obtained using the Hreco method. The validation of our process is depicted in Figure 3.13, where it is evident that the unfolded distribution closely aligns with the truth distribution. This alignment confirms the successful correction of detector effects.

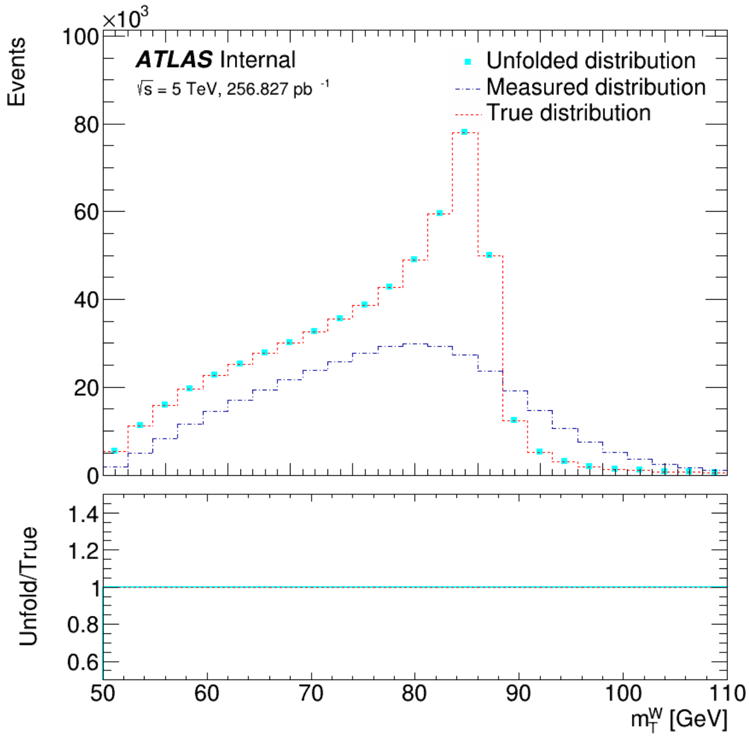

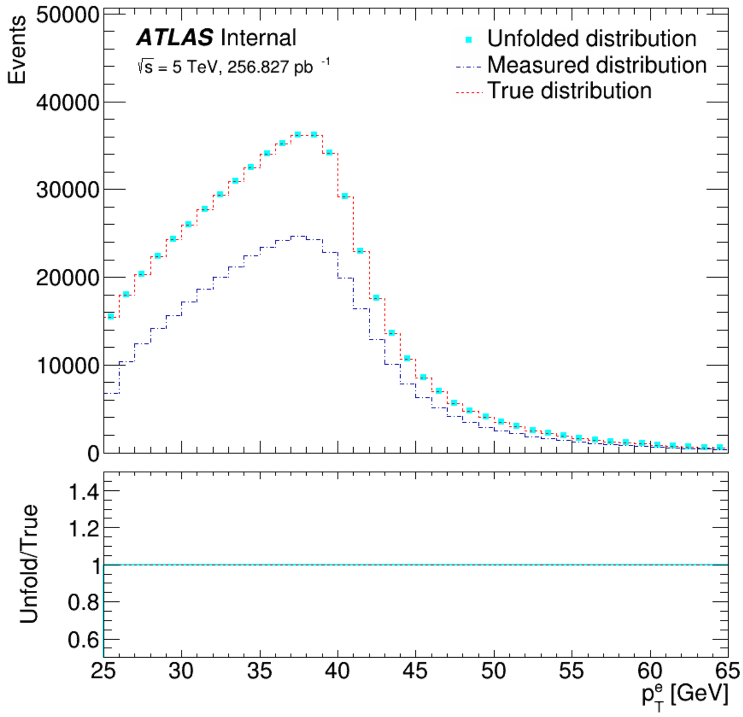

Figure 3.13: p_T^e & m_T^W distributions before and after detector effects, with the unfolded distributions, The lower panel illustrates the ratio of the unfolded distributions compared to the true distributions.

3.6.4 Uncertainties with unfolding : Propagation of the statistical uncertainty

The propagation of statistical uncertainties in the unfolding process involves the use of pseudo-data[33], commonly referred to as toys. In the case of the closure test, the simulated reconstructed distribution is utilized as the unfolding input.These toys are generated by fluctuating the data distributions, employing Poisson variations[78], resulting in multiple variations of the input.The unfolding procedure is then performed on each toy, utilizing our migration matrix. By comparing the unfolded distributions obtained from each toy, the covariance matrix for the statistical uncertainty is calculated:

$$\mathrm{Cov}(i,j) = \frac{1}{n-1}\sum_{k=1}^{n}(X_i^k - \bar{X}_i)(X_j^k - \bar{X}_j)^T \tag{3.13}$$

where $X_i^k \left(X_j^k\right)$ corresponds to the content of bin i(j) of the unfolded toy k, $\bar{X}_i(\bar{X}_j)$ corresponds to the content of bin i(j) of the average of all toys.Thus the elements of the covariance matrix represent the covariance between two bins, indicating how the statistical uncertainties of these two bins are interrelated. To calculate the correlation matrix between bins for the statistical uncertainty, the covariance matrix is utilized, employing the following formula:

$$Corr(i,j) = \frac{Cov(i,j)}{\sqrt{Cov(i,i)} \times \sqrt{Cov(j,j)}}. \tag{3.14}$$

Figure 3.15 illustrates the covariance matrix obtained through the Ereco method, along with the correlation matrix. These matrices represent the statistical uncertainty of the unfolding distribution. It is worth noting that, for the observable p_T^e, there is a noticeable lack of correlation among the bins, indicating a weak interdependence between them. On the other hand, for the observable m_T^W, there is a significant correlation between the bins.

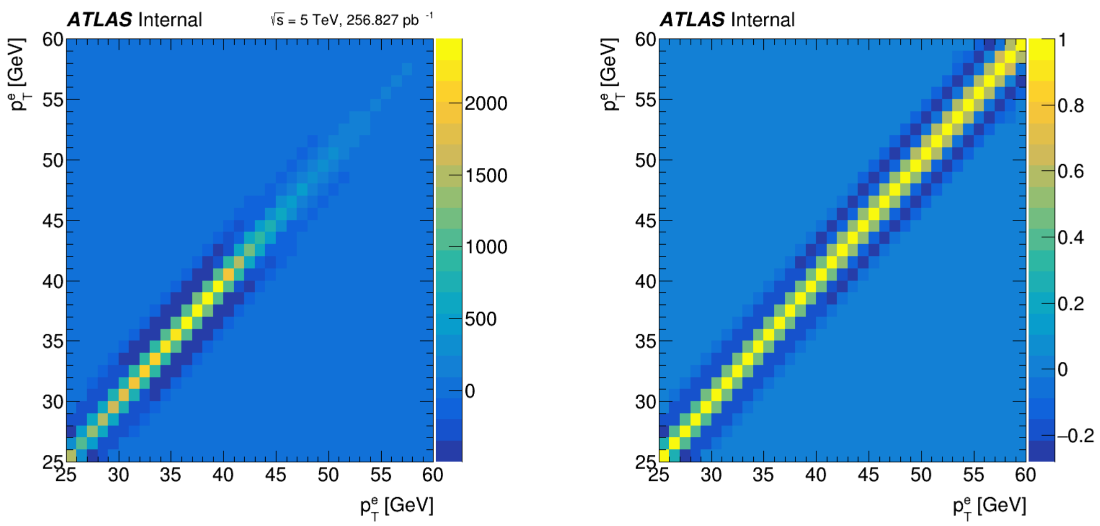

Figure 3.14: Example of the covariance matrix (left) and the correlation matrix (right) for the the statistical uncertainty of the unfolding distribution for the observable p_T^e.

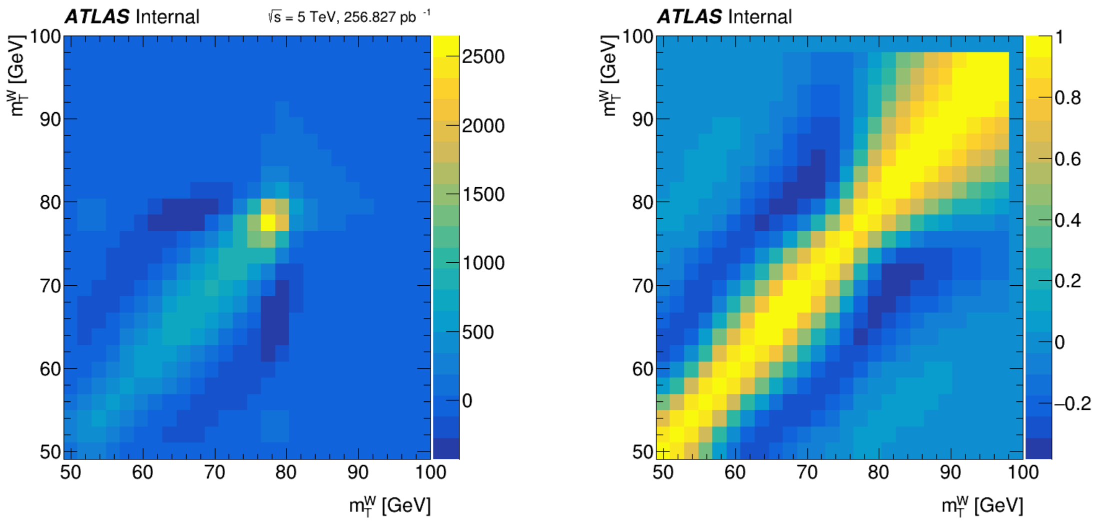

Figure 3.15: Example of the covariance matrix (left) and the correlation matrix (right) for the the statistical uncertainty of the unfolding distribution for the observable m_T^W.

3.6.5 W boson mass using the unfolded distribution

After introducing the unfolding procedure and verifying its consistency through the closure test, in this section, our attention turns to the precise measurement of the W boson's mass using unfolded distributions that have already been corrected by the unfolding procedure and do not contain undesirable detector effects. The determination of the W boson mass is the same as described with the template method. However, there is a modification in the calculation of the χ^2 formula to account for the correlation between bins at the unfolded level, which is introduced by the unfolding procedure. The updated χ^2 formula is given by:

$$\chi^2 = \left(n_{\text{data}}^{Unf} - n_{\text{template}}^{Unf}\right)^T \cdot \left(V_{\text{data}} + V_{\text{template}}\right)^{-1} \cdot \left(n_{\text{data}}^{Unf} - n_{\text{template}}^{Unf}\right) \tag{3.15}$$

Where: n_{data}^{Unf} ($n_{\text{template}}^{Unf}$) represents the unfolded distribution of the data(template), and V_{data} (V_{template}) represents the covariance matrix of the statistical uncertainty for the unfolded distribution of data (template). The calculation of V_{data} and V_{template} is explained in detail in subsection3.6.4.

In this analysis, we utilized the iterative Bayesian unfolding method explained in subsections3.6.2, 3.6.3 to unfold the m_T^W and p_T^e distributions. Additionally, we applied the same unfolding procedure to the template distributions using the corresponding migration matrix. Our analysis involved 11 templates that were previously employed in the template method discussed in earlier sections. Figure 3.16 provides an example of the unfolded templates along with the unfolded nominal distribution for the observable p_T^e. Then, the covariance matrices for the statistical uncertainty of the unfolded distributions were calculated using the RooUnfold framework, as detailed in subsection3.6.2, 3.6.3. Figure 3.17 demonstrates an example of the covariance matrices for the distribution dM-200Mev for both observables m_T^W and p_T^e. Ultimately, for both the m_T^W and p_T^e observables, we obtained 11 templates and the nominal distribution, all at the unfolded level, along with their corresponding covariance matrices. All of these unfolded distributions were saved in a root file and are used for the calculation of the χ^2.

The comparison between the data and the templates is conducted using the new χ^2 formula, described by equation 3.15.The procedure follows a similar approach to the template method explained in Sections3.3, 3.4.The obtained results are presented in Figure 3.18. Finally, the W boson mass is extracted along with its statistical uncertainty, as summarized in Table 3.4.

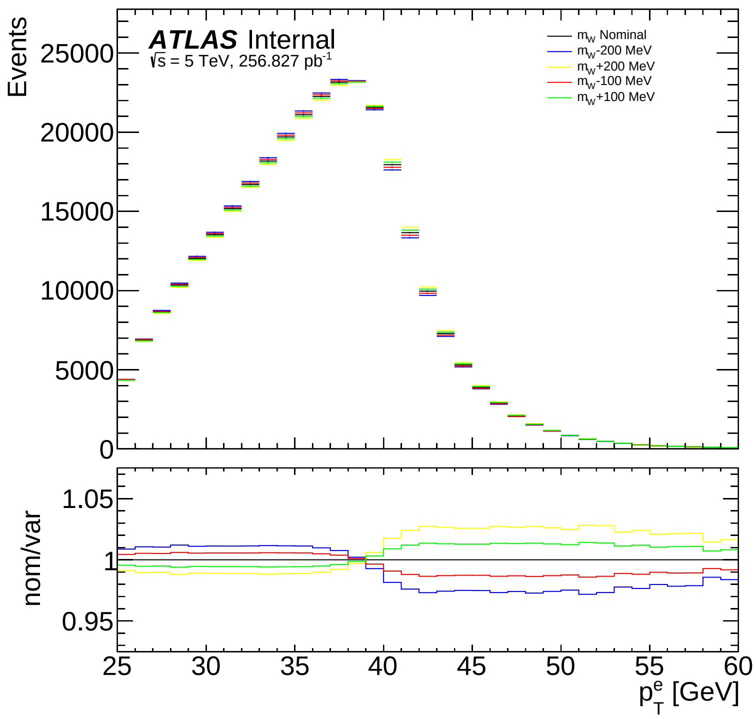

Figure 3.16: Distributions of p_T^e with their corresponding templates at the unfolded level are shown. The lower panel displays the ratio of the unfolded templates to the unfolded nominal distribution.

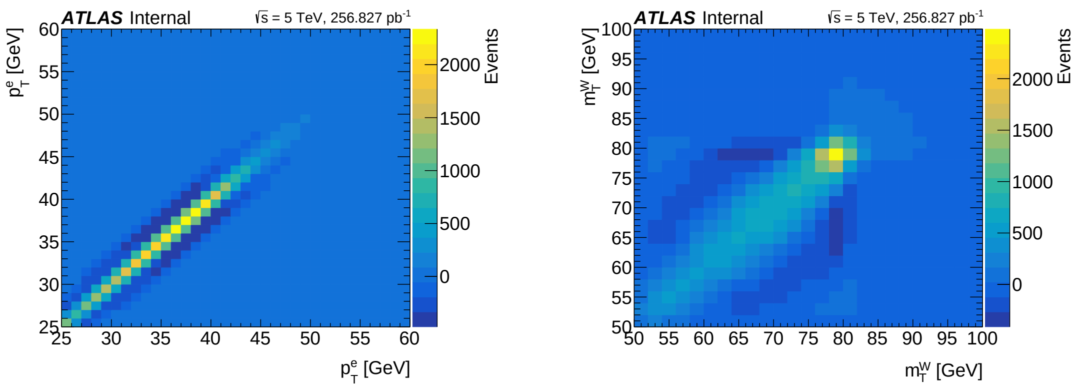

Figure 3.17: Covariance matrices for the statistical uncertainty for m_T^W (right) and p_T^e (left) distributions at the unfolded level.

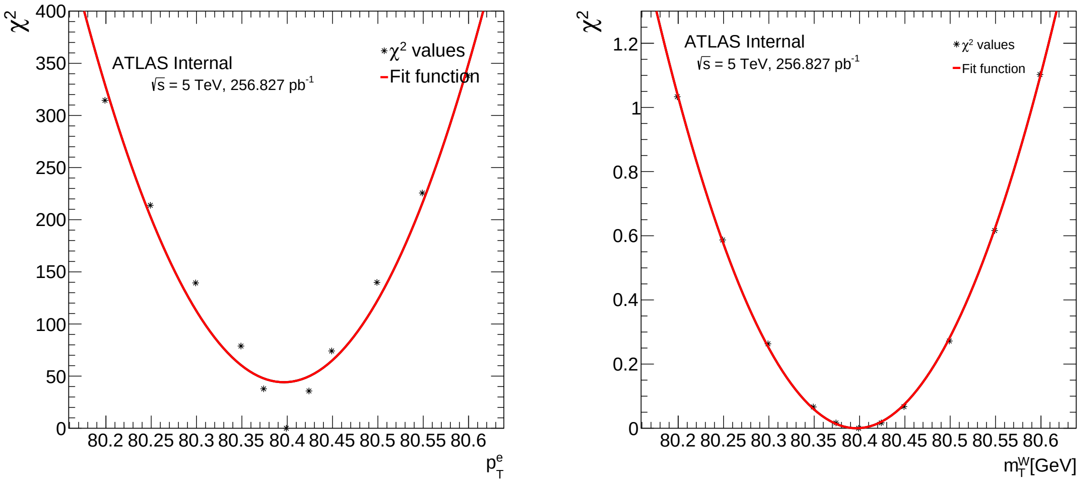

Figure 3.18: Fitting the χ^2 distribution of m_T^W (right) and p_T^e (left) with a parabola (red line) using different MC templates (11 templates), at the unfolded level. The minimum of the χ^2 corresponds to the extracted mass value.

	$m_{\mathrm{T}}^{\mathrm{W}} \pm \sigma_{stat}$	$p_{\mathrm{T}}^{e} \pm \sigma_{stat}$
Channel	$W^+ \to e^+\nu_e$	
MC	80.396 ± 0.193	80.399 ± 0.018

Table 3.4: The values of the W boson mass, along with their corresponding statistical uncertainties, for the two observables m_T^W and p_T^e, expressed in GeV.

During this chapter, we employed two approaches for measuring the mass of the W boson. The first approach was the template method, which utilized distributions at the reconstructed level. The second approach involved utilizing distributions at the unfolded level. The underlying concept of the latter method was to utilize distributions that had already been corrected by the unfolding procedure and were free from undesirable detector effects. The extraction of the W boson mass is similar to the template method. However, the unfolded distributions have a particular characteristic in that the unfolding procedure introduces a correlation between bins. This correlation is taken into account in the χ^2 formula.

We can conclude that the template method is the best strategy for determining the W boson mass. Therefore, compared to the unfolded distributions, the reconstructed distributions are more sensitive to the W boson mass. Generally, using the unfolded distribution does not change the results for the statistical uncertainties.

Conclusion

This work presents the measurement of the W boson mass using the ATLAS detector at the LHC. The analysis is based on a low pile-up data set collected by ATLAS in 2017 during Run 2, corresponding to an integrated luminosity of 256.827 pb^{-1} at $\sqrt{s} = 5\ TeV$. The measurement is performed by fitting templates to the transverse momentum distributions of charged leptons and the transverse mass distributions of the W boson in the electron decay mode.

The first chapter described the theoretical context that sets up the study for our particle physics process, beginning with the most fundamental model, the Standard Model of particle physics, and moving on to specific aspects of the W boson, such as its properties, production, and decay modes. Furthermore, a brief historical account of W boson mass measurements is presented, with a particular focus on the latest results published by the ATLAS collaboration.

The second chapter provided a detailed account of the experimental setup used for data collection in this study, from the LHC acceleration chain at CERN to various compartments and detectors within the ATLAS experiment. Furthermore, we discuss the reconstruction of crucial objects that contribute significantly to determining the mass of the W boson, including electrons, muons, missing transverse energy, and the hadronic recoil

In the third and final chapter, we presented the results of our data analysis. First, we presented the sources of our data and Monte Carlo (MC) samples, the selections applied, and we explained the measurement strategy. After that we measured the W boson mass using two different approaches :

The template method involves generating simulated Monte Carlo (MC) distributions of m_T^W and p_T^e for different assumed values of m_W (templates). The comparison between the templates and the data is used to determine the best value for the W boson mass using the χ^2 test.

In addition to the template method, this study also employs an alternative approach using unfolded distributions instead of reconstructed ones. The main idea is to use distributions that have been corrected by the unfolding procedure and are free from undesirable detector effects. The W boson mass and the sources of statistical uncertainties are calculated separately using the m_T^W and p_T^e distributions, and then combined to obtain the final result. Since the distributions of interest are generated from the same events, the correlation between these two variables is taken into account, and it is calculated using MC toys.

This work presents the measurement of the W boson mass using both of these approaches, which have the same principle. However, in the second method, the χ^2 formula is modified to account for the correlation between bins introduced by the unfolding procedure. We concluded that the template method emerges as the optimal approach for determining the mass of the W boson. Consequently, the reconstructed distributions exhibit greater sensitivity to the W boson mass in comparison to the unfolded distributions. Typically, employing the unfolded distribution maintains the results within the realm of statistical uncertainties.

Bibliography

[1] Sheldon L Glashow. “Partial-symmetries of weak interactions”. In: *Nuclear physics* 22.4 (1961), pp. 579–588.
[2] Steven Weinberg. “Stephen Weinberg”. In: *Quantum Algebra and Symmetry* (2010), p. 665.
[3] Salam Abdus. “Weak and electromagnetic interactions, conf”. In: *Proc. C* 680519 (1968), pp. 367–377.
[4] David Griffiths. *Introduction to elementary particles*. John Wiley & Sons, 2020.
[5] C. S. Unnikrishnan. *Bosons, Fermions, Spin, Gravity, and the Spin-Statistics Connection*. 2019. arXiv: 1906.07656 [physics.pop-ph].
[6] Juerg Beringer et al. “Review of particle physics”. In: *Physical Review D* 86.1 (2012).
[7] Jean-Marc Richard. *An introduction to the quark model*. 2012. arXiv: 1205.4326 [hep-ph].
[8] Vladimir Borisovich Berestetskii, Evgenii Mikhailovich Lifshitz, and Lev Petrovich Pitaevskii. *Quantum Electrodynamics: Volume 4*. Vol. 4. Butterworth-Heinemann, 1982.
[9] Andrey Grozin. “Quantum Chromodynamics”. In: *arXiv preprint arXiv:1205.1815* (2012).
[10] VA Bednyakov, ND Giokaris, and AV Bednyakov. “On the Higgs mass generation mechanism in the Standard Model”. In: *Physics of Particles and Nuclei* 39 (2008), pp. 13–36.
[11] Anne Kernan. “The Discovery of the Intermediate Vector Bosons: Predicted by theory since the 1960s, the W and Z particles were beyond the reach of existing accelerators and detectors”. In: *American Scientist* 74.1 (1986), pp. 21–28.
[12] Steven D Bass, Albert De Roeck, and Marumi Kado. “The Higgs boson implications and prospects for future discoveries”. In: *Nature Reviews Physics* 3.9 (2021), pp. 608–624.
[13] Sidney D Drell and Tung-Mow Yan. “Massive lepton-pair production in hadron-hadron collisions at high energies”. In: *Physical Review Letters* 25.5 (1970), p. 316.
[14] Maarten Boonekamp, Stefan Dittmaier, and Matthias Mozer. “Electroweak Standard Model Physics”. In: *The Large Hadron Collider: Harvest of Run 1*. Springer, 2015, pp. 95–138.
[15] Elisabeth E Petit. “Première mesure de section efficace de production du boson W et de son asymétrie de charge avec l’expérience ATLAS”. PhD thesis. Université de la Méditerranée-Aix-Marseille II, 2011.
[16] Christoph Schäfer. “The Z lineshape at LEP”. In: *Nuclear Physics B-Proceedings Supplements* 65.1-3 (1998), pp. 93–97.
[17] Robin G Stuart. “An Improved Determination of the Fermi Coupling Constant, G_F”. In: *arXiv preprint hep-ph/9902257* (1999).
[18] Jonas Rademacker. “Review of Particle Physics (2018)”. In: *Physical Review D* 98.3 (2018), p. 030001.
[19] Masaharu Tanabashi et al. “Review of Particle Physics: particle data groups”. In: *Physical Review D* 98.3 (2018), pp. 1–1898.

[20] Gfitter Group et al. "The global electroweak fit at NNLO and prospects for the LHC and ILC". In: *The European Physical Journal C* 74 (2014), pp. 1–14.

[21] Marina Béguin. "Calorimetry and W mass measurement for future experiments". PhD thesis. Université Paris-Saclay (ComUE), 2019.

[22] Rémie Hanna. "Contributions to a first measurement of the W-boson mass in the electron channel with the ATLAS detector". PhD thesis. Université Paris Sud-Paris XI, 2015.

[23] KA Olive et al. "Review of particle physics". In: *Chinese physics C* 38.9 (2014), pp. 1–1676.

[24] Timo Aaltonen et al. "Precise measurement of the W-boson mass with the CDF II detector". In: *Physical review letters* 108.15 (2012), p. 151803.

[25] Victor Mukhamedovich Abazov et al. "Measurement of the W Boson Mass with the D0 Detector". In: *Physical review letters* 108.15 (2012), p. 151804.

[26] Morad Aaboud et al. "Measurement of the W-boson mass in pp collisions at

\sqrt {s}= 7\,\hbox {TeV}

$$s = 7TeVwiththeATLASdetector$$

". In: *The European Physical Journal C* 78.2 (2018), pp. 1–61.

[27] ATLAS Collaboration et al. "Improved W boson Mass Measurement using s= 7 TeV Proton-Proton Collisions with the ATLAS Detector". In: ATLAS-CONF-2023-004. 2023.

[28] CDF Collaboration†‡ et al. "High-precision measurement of the W boson mass with the CDF II detector". In: *Science* 376.6589 (2022), pp. 170–176.

[29] Ana Lopes and Melissa Loyse Perrey. "FAQ-LHC The guide". 2022. url: `https://cds.cern.ch/record/2809109`.

[30] B.J. Holzer. "Introduction to Particle Accelerators and their Limitations". en. In: *CERN Yellow Reports* (2016), Vol 1 (2016): Proceedings of the 2014 CAS–CERN Accelerator School: Plasma Wake Acceleration. doi: `10.5170/CERN-2016-001.29`. url: `https://e-publishing.cern.ch/index.php/CYR/article/view/212`.

[31] C.E. Gerber. "LHC highlights and prospects". en. In: *CERN Yellow Reports: School Proceedings* Vol. 2 (2021 2021), 13–26 March 2019. doi: `10.23730/CYRSP-2021-002.161`. url: `https://e-publishing.cern.ch/index.php/CYRSP/article/view/1314`.

[32] Ewa Lopienska. "The CERN accelerator complex, layout in 2022. Complexe des accélérateurs du CERN en janvier 2022". In: (2022). General Photo. url: `https://cds.cern.ch/record/2800984`.

[33] Hicham Atmani. "Étalonnage du calorimètre électromagnétique ATLAS et mesure des propriétés du Boson W à s= 5 et 13 TeV avec le détecteur ATLAS au LHC." PhD thesis. Université Paris-Saclay, 2020.

[34] *Luminosity determination in pp collisions at $\sqrt{s} = 13$ TeV using the ATLAS detector at the LHC*. Tech. rep. All figures including auxiliary figures are available at https://atlas.web.cern.ch/Atlas/GROUPS/PHYSICS/CONFNOTES/ATLAS-CONF-2019-021. Geneva: CERN, 2019. url: `https://cds.cern.ch/record/2677054`.

[35] Tadej Novak. "ATLAS Pile-up and Overlay Simulation". In: (2017). url: `https://cds.cern.ch/record/2270396`.

[36] The ATLAS Collaboration. "The ATLAS Experiment at the CERN Large Hadron Collider". In: *Journal of Instrumentation* 3.08 (Aug. 2008), S08003. doi: 10.1088/1748-0221/3/08/S08003. url: https://dx.doi.org/10.1088/1748-0221/3/08/S08003.

[37] The CMS Collaboration. "The CMS experiment at the CERN LHC". In: *Journal of Instrumentation* 3.08 (Aug. 2008), S08004. doi: 10.1088/1748-0221/3/08/S08004. url: https://dx.doi.org/10.1088/1748-0221/3/08/S08004.

[38] The LHCb Collaboration. "The LHCb Detector at the LHC". In: *Journal of Instrumentation* 3.08 (Aug. 2008), S08005. doi: 10.1088/1748-0221/3/08/S08005. url: https://dx.doi.org/10.1088/1748-0221/3/08/S08005.

[39] The ALICE Collaboration. "The ALICE experiment at the CERN LHC". In: *Journal of Instrumentation* 3.08 (Aug. 2008), S08002. doi: 10.1088/1748-0221/3/08/S08002. url: https://dx.doi.org/10.1088/1748-0221/3/08/S08002.

[40] *Glossary*. http://opendata.atlas.cern/books/current/get-started/_book/GLOSSARY.html. Accessed: 2023-06-12.

[41] ATLAS Outreach. "ATLAS Fact Sheet : To raise awareness of the ATLAS detector and collaboration on the LHC". 2010. doi: 10.17181/CERN.1LN2.J772. url: https://cds.cern.ch/record/1457044.

[42] The ATLAS Collaboration. "The ATLAS Inner Detector commissioning and calibration". In: *The European Physical Journal C* 70 (Dec. 2010), pp. 787–821. doi: 10.1140/epjc/s10052-010-1366-7.

[43] M.S Alam et al. "The ATLAS silicon pixel sensors". In: *Nuclear Instruments and Methods in Physics Research Section A: Accelerators, Spectrometers, Detectors and Associated Equipment* 456.3 (2001), pp. 217–232. issn: 0168-9002. doi: https://doi.org/10.1016/S0168-9002(00)00574-X. url: https://www.sciencedirect.com/science/article/pii/S016890020000574X.

[44] Georges Blanchot et al. "The Cesium source calibration and monitoring system of the ATLAS Tile Calorimeter: design, construction and results". In: *Journal of Instrumentation* 15 (Mar. 2020), P03017–P03017. doi: 10.1088/1748-0221/15/03/P03017.

[45] *ATLAS liquid-argon calorimeter: Technical Design Report*. Technical design report. ATLAS. Geneva: CERN, 1996. doi: 10.17181/CERN.FWRW.FOOQ. url: https://cds.cern.ch/record/331061.

[46] Carlos Solans Sanchez, Juan Ferrer, and Emilio Higon-Rodriguez. "Implementation of the ROD Crate DAQ Software for the ATLAS Tile Calorimeter and a Search for a MSSM Higgs Boson decaying into Tau pairs". In: (Jan. 2010).

[47] The ATLAS Collaboration. "Readiness of the ATLAS Tile Calorimeter for LHC collisions". In: *European Physical Journal C* (Jan. 2010).

[48] Jessica Metcalfe et al. "Development of Planar and 3D Silicon Sensor Technologies for the ATLAS Experiment Upgrades and Measurements of Heavy Quark Production Fractions with Fully Reconstructed D-star Mesons with ATLAS". In: (June 2023).

[49] *ATLAS level-1 trigger: Technical Design Report*. Technical design report. ATLAS. Geneva: CERN, 1998. url: http://cds.cern.ch/record/381429.

[50] Peter Jenni et al. *ATLAS high-level trigger, data-acquisition and controls: Technical Design Report*. Technical design report. ATLAS. Geneva: CERN, 2003. url: https://cds.cern.ch/record/616089.

[51] Jose Guillermo Panduro Vazquez. "The ATLAS Data Acquisition System in LHC Run 2". In: *Journal of Physics: Conference Series* 898 (Oct. 2017), p. 032017. doi: 10.1088/1742-6596/898/3/032017.

[52] A Ruiz Martınez, ATLAS Collaboration, et al. "The run-2 ATLAS trigger system". In: *Journal of Physics: Conference Series*. Vol. 762. 1. IOP Publishing. 2016, p. 012003.

[53] *ATLAS Computing: technical design report*. Technical design report. ATLAS. Geneva: CERN, 2005. url: https://cds.cern.ch/record/837738.

[54] K. Bos et al. *LHC computing Grid: Technical Design Report. Version 1.06 (20 Jun 2005)*. Technical design report. LCG. Geneva: CERN, 2005. url: https://cds.cern.ch/record/840543.

[55] The ATLAS Collaboration. "The ATLAS Simulation Infrastructure". In: *The European Physical Journal C* 70.3 (Sept. 2010), pp. 823–874. doi: 10.1140/epjc/s10052-010-1429-9. url: https://doi.org/10.1140/epjc/s10052-010-1429-9.

[56] S. Agostinelli et al. "Geant4—a simulation toolkit". In: *Nuclear Instruments and Methods in Physics Research Section A: Accelerators, Spectrometers, Detectors and Associated Equipment* 506.3 (2003), pp. 250–303. issn: 0168-9002. doi: https://doi.org/10.1016/S0168-9002(03)01368-8. url: https://www.sciencedirect.com/science/article/pii/S0168900203013688.

[57] Elzbieta Richter-Was, D Froidevaux, and Luc Poggioli. *ATLFAST 2.0 a fast simulation package for ATLAS*. Tech. rep. Geneva: CERN, 1998. url: https://cds.cern.ch/record/683751.

[58] E Barberio et al. "Fast shower simulation in the ATLAS calorimeter". In: *Journal of Physics: Conference Series* 119.3 (July 2008), p. 032008. doi: 10.1088/1742-6596/119/3/032008. url: https://dx.doi.org/10.1088/1742-6596/119/3/032008.

[59] Daniela Maria Kock. "Search for charginos and neutralinos decaying via a W and a Higgs boson into final states with two same-sign leptons with the ATLAS detector". PhD thesis. Munich U.

[60] Joao Pequenao and Paul Schaffner. "An computer generated image representing how ATLAS detects particles". In: *accessed* 28 (2013), p. 2015.

[61] ATLAS Collaboration atlas. publications@ cern. ch et al. "Measurement of the muon reconstruction performance of the ATLAS detector using 2011 and 2012 LHC proton–proton collision data". In: *The European Physical Journal C* 74 (2014), pp. 1–34.

[62] The ATLAS Collaboration. "Electron reconstruction and identification in the ATLAS experiment using the 2015 and 2016 LHC proton–proton collision data at \sqrt{s} = 13 \text {TeV}". In: *The European Physical Journal C* 79.8 (Aug. 2019). doi: 10.1140/epjc/s10052-019-7140-6. url: https://doi.org/10.1140/epjc/s10052-019-7140-6.

[63] *Electron and photon reconstruction and performance in ATLAS using a dynamical, topological cell clustering-based approach*. Tech. rep. All figures including auxiliary figures are available at https://atlas.web.cern.ch/Atlas/GROUPS/PHYSICS/PUBNOTES/ATL-PHYS-PUB-2017-022. Geneva: CERN, 2017. url: https://cds.cern.ch/record/2298955.

[64] Philipp Konig. "Measurement of mass and width of the W-boson, and test of lepton universality in W-boson decays with the ATLAS detector". Presented 09 Feb 2023. 2022. url: https://cds.cern.ch/record/2856832.

[65] Mengran Li et al. *Hadronic recoil reconstruction and calibration for low pile-up runs taken in 2017 and 2018*. Tech. rep. Geneva: CERN, 2019. url: https://cds.cern.ch/record/2657182.

[66] Oleh Kivernyk. "Measurement of the W boson mass with the ATLAS detector". Presented 19 Sep 2016. 2017. url: https://cds.cern.ch/record/2262454.

[67] G Apollinari et al. *High-Luminosity Large Hadron Collider (HL-LHC): Preliminary Design Report*. CERN Yellow Reports: Monographs. Geneva: CERN, 2015. doi: 10.5170/CERN-2015-005. url: http://cds.cern.ch/record/2116337.

[68] Hassnae El Jarrari. *Performance of LGAD sensors for the ATLAS High-Granularity Timing Detector HGTD*. Tech. rep. ATL-COM-HGTD-2021-026, 2021.

[69] Nansi Andari et al. *Measurement of mW with 7 TeV data: W boson mass measurement*. Tech. rep. Tech. rep. ATL-COM-PHYS-2014-1569. Geneva: CERN, 2014.

[70] Jan Kretzschmar et al. *Samples and Physics modelling for low pile-up runs taken in 2017 and 2018*. Tech. rep. Geneva: CERN, 2019. url: https://cds.cern.ch/record/2657141.

[71] Samik Raychaudhuri. "Introduction to monte carlo simulation". In: *2008 Winter simulation conference*. IEEE. 2008, pp. 91–100.

[72] Volker Blobel. "Unfolding Methods in Particle Physics". In: (2011), pp. 240–251. doi: 10.5170/CERN-2011-006.240. url: https://cds.cern.ch/record/2203257.

[73] J.W. Monk and C. Oropeza-Barrera. "The HBOM method for unfolding detector effects". In: *Nuclear Instruments and Methods in Physics Research Section A: Accelerators, Spectrometers, Detectors and Associated Equipment* 701 (2013), pp. 17–24. issn: 0168-9002. doi: https://doi.org/10.1016/j.nima.2012.09.045. url: https://www.sciencedirect.com/science/article/pii/S0168900212011023.

[74] Stefan Schmitt. "Data unfolding methods in high energy physics". In: *EPJ web of conferences*. Vol. 137. EDP Sciences. 2017, p. 11008.

[75] Georgios Choudalakis. "Fully bayesian unfolding". In: *arXiv preprint arXiv:1201.4612* (2012).

[76] Tim Adye. *Unfolding algorithms and tests using RooUnfold*. 2011. arXiv: 1105.1160 [physics.data-an].

[77] G. D'Agostini. *Improved iterative Bayesian unfolding*. 2010. arXiv: 1010.0632 [physics.data-an].

[78] S.I. Bityukov and N.V. Krasnikov. "Signal significance in the presence of systematic and statistical uncertainties". In: *Nuclear Instruments and Methods in Physics Research Section A: Accelerators, Spectrometers, Detectors and Associated Equipment* 502.2-3 (Apr. 2003), pp. 795–798. doi: 10.1016/s0168-9002(03)00586-2. url: https://doi.org/10.1016%2Fs0168-9002%2803%2900586-2.

Appendix A

DATA & MC χ^2 distributions

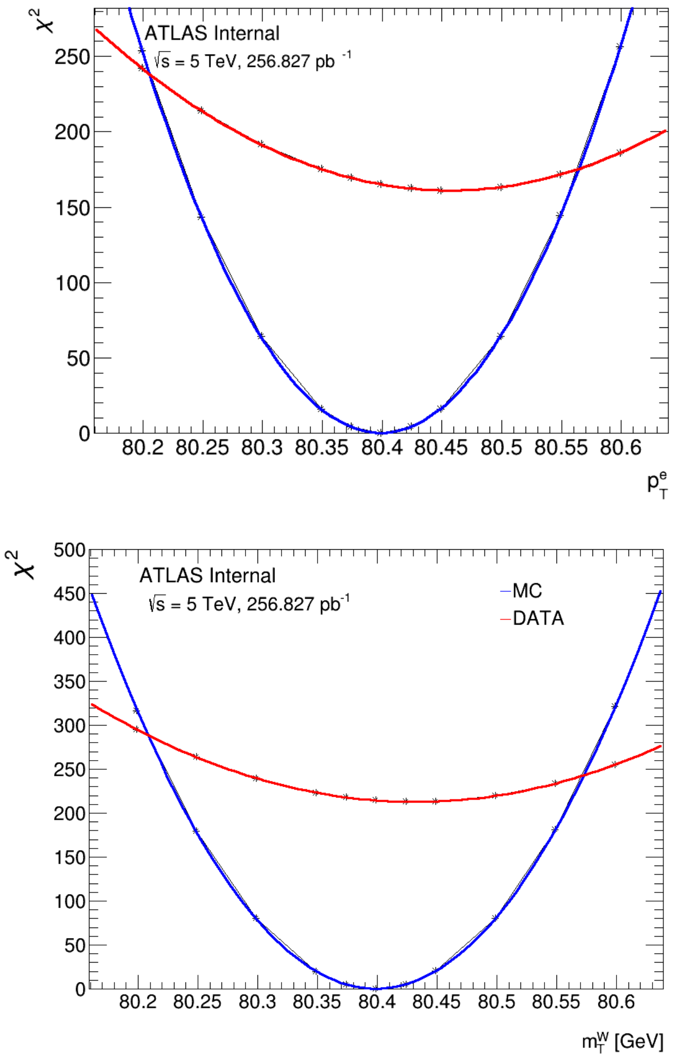

Figure A.1: Comparison between Data and MC χ^2 distributions for p_T^e (left) and m_T^W (right).

Appendix B

Templates at the unfolded level

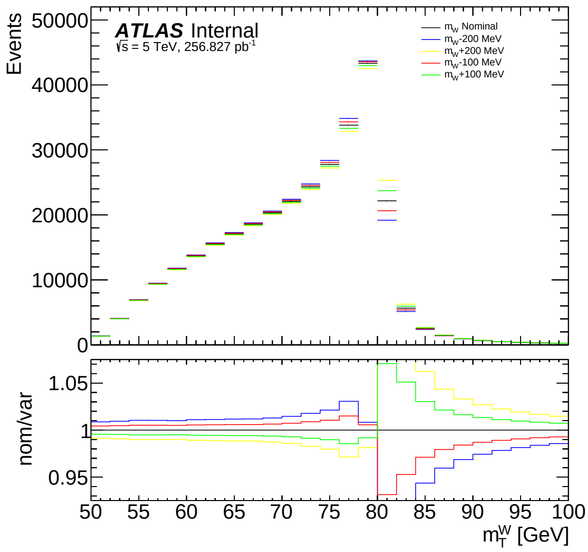

Figure B.1: Distributions of m_T^W with their corresponding templates at the unfolded level are shown. The lower panel displays the ratio of the unfolded templates to the unfolded nominal distribution.